JGR Planets

RESEARCH ARTICLE

10.1029/2024JE008582

Re-Analysis of Pioneer Venus Data: Water, Iron Sulfate, and Sulfuric Acid are Major Components in Venus' Aerosols

R. Mogul[1,2], M. Yu. Zolotov[3], M. J. Way[4,5], and S. S. Limaye[6]

[1]Chemistry & Biochemistry Department, California State Polytechnic University, Pomona, CA, USA, [2]Blue Marble Institute of Science, Seattle, WA, USA, [3]School of Earth and Space Exploration, Arizona State University, Tempe, AZ, USA, [4]NASA Goddard Institute for Space Studies, New York, NY, USA, [5]Department of Physics and Astronomy, Theoretical Astrophysics Group, Uppsala University, Uppsala, Sweden, [6]University of Wisconsin, Madison, WI, USA

Key Points:

- The Pioneer Venus Large Probe results were re-interpreted as the thermal and evolved gas analysis of aerosol composition
- Venus' aerosols from the middle and lower clouds contain substantial water, iron sulfate, and sulfuric acid
- Thermal decomposition of the aerosols released sufficient water to yield hydrates of ferric sulfate, magnesium sulfate, and other species

Correspondence to:

R. Mogul,
rmogul@cpp.edu

Citation:

Mogul, R., Zolotov, M. Y., Way, M. J., & Limaye, S. S. (2025). Re-analysis of Pioneer Venus data: Water, iron sulfate, and sulfuric acid are major components in Venus' aerosols. *Journal of Geophysical Research: Planets*, *130*, e2024JE008582. https://doi.org/10.1029/2024JE008582

Received 26 JUN 2024
Accepted 28 AUG 2025

Author Contributions:

Conceptualization: R. Mogul, M. Yu. Zolotov
Data curation: R. Mogul, M. J. Way
Formal analysis: R. Mogul
Funding acquisition: R. Mogul
Investigation: R. Mogul, M. Yu. Zolotov, M. J. Way, S. S. Limaye
Methodology: R. Mogul
Project administration: R. Mogul
Visualization: R. Mogul
Writing – original draft: R. Mogul
Writing – review & editing: R. Mogul, M. Yu. Zolotov, M. J. Way, S. S. Limaye

Abstract We present a new and transformative composition for Venus' cloud aerosols using previously uncharacterized data acquired by the Pioneer Venus Large Probe, which descended through Venus' atmosphere in 1978. This aerosol composition was extracted by re-analyzing data acquired by the Large Probe Neutral Mass Spectrometer (LNMS) and re-evaluating results from the Large Probe Gas Chromatograph (LGC). In our approach, the altitude-based data from the LNMS and LGC were re-interpreted as the thermal and evolved gas analysis of aerosol composition. During the descent, the LNMS and LGC inadvertently collected cloud aerosols and subsequently measured the release of gases and compounds as the captured aerosols thermally decomposed across the hot sub-cloud atmosphere. Evolved compounds that were released into the LNMS included SO_2, H_2O, SO_3, O_2, and likely Fe_2O_3 and $MgSO_4$. Evolved gases that were released into the LGC included SO_2, H_2O, and O_2, which likely formed during the programmed LGC heating steps. These results are consistent with the thermal decomposition of aerosols containing comparable masses of ferric sulfate and sulfuric acid (~20 wt%, each) and sufficiently high H_2O abundances (~60 wt%) to yield hydrated iron sulfates, hydrated magnesium sulfate, and other hydrates. We suggest that iron and magnesium could originate from cosmic sources. Our comparisons indicate that aerosol H_2O was also measured by direct analyses on the Venera and Vega probes. Hence, this work reveals reservoirs of water and possible altered cosmic materials in the aerosols, which presents new considerations for cloud chemistry and cloud habitability models.

Plain Language Summary We present a new and transformative composition for the aerosols in Venus' clouds. This information was obtained by analysis of previously uncharacterized data acquired by the Pioneer Venus (PV) Large Probe, which descended through Venus' atmosphere in 1978. Our findings support the assessment that aerosols were captured in the clouds and subsequently decomposed and released several gases and compounds into the onboard instruments as the PV Large Probe descended through the hot sub-cloud atmosphere. The released gases and compounds indicate that the cloud aerosols contain several major species, including substantial bulk water and comparable masses of ferric sulfate and sulfuric acid. The aerosol water likely arises from hydrates, including hydrated iron and magnesium sulfates. We suggest that iron and magnesium could originate from cosmic sources. We additionally propose that the Soviet Vega and Venera probes also measured the substantial aerosol water. This work significantly expands on the original PV Large Probe studies and reveals reservoirs of water and possible cosmic materials in the aerosols. Hence, these results yield new considerations for cloud chemistry models and cloud habitability discussions.

1. Introduction

In this report, we present new and transformative insights into the composition of Venus' aerosols using previously uncharacterized data acquired by the Pioneer Venus Large Probe (PVLP), which descended through Venus' atmosphere in 1978 (Fimmel, 1983). The aerosols in Venus' clouds play intricate roles in the atmospheric chemical processes and thermal balance of the planet (Esposito et al., 1997; Mills et al., 2007; Titov et al., 2018). During the descent of the PVLP, the onboard instruments inadvertently collected these cloud aerosols and measured the decomposition of their contents (Hoffman, Hodges, Donahue, & McElroy, 1980). In the initial post-flight PVLP investigations, aerosol collection and analysis were inferred for the Large Probe Neutral Mass Spectrometer (LNMS) (Hoffman, Hodges, Donahue, & McElroy, 1980) and considered for the Large Probe Gas Chromatograph (LGC) (Oyama et al., 1979a, 1979b; Oyama, Carle, Woeller, Pollack et al., 1980).

For the LNMS, the inadvertent capture of aerosols resulted in clogging of the inlets and significant though temporary losses in the intake of atmospheric gases (Hoffman, Hodges, Donahue, & McElroy, 1980; Mogul, Limaye & Way, 2023). Notably, the resumption of atmospheric intake into the LNMS, which occurred in the hot sub-cloud atmosphere, coincided with substantial increases in the measured SO_2 and H_2O. In the original LNMS investigations (Hoffman, Hodges, Donahue, & McElroy, 1980), and in our recent analysis of the archived LNMS data (Mogul, Limaye & Way, 2023), this release of SO_2 and H_2O during the clog was attributed to the thermal decomposition of sulfuric acid (H_2SO_4) from the captured aerosols.

Multiple lines of evidence suggest that the cloud aerosols contain a concentrated water solution of H_2SO_4 (≥75%, by mass). Direct measurements for aerosol-phase H_2SO_4 include the LNMS (Hoffman, Hodges, Donahue, & McElroy, 1980), reaction gas chromatography on Vega 1 and 2 (Gel'man et al., 1986; Porshnev et al., 1987), and pyrolysis mass spectrometry on Vega 1 (Surkov, Ivanova et al., 1986). Spectral or indirect measurements for aerosol-phase H_2SO_4 include remote polarimetry (Barstow et al., 2012; Hansen & Hovenier, 1974), in situ polarimetry on the Pioneer Venus (PV) descent probes (Knollenberg & Hunten, 1980), and orbital and telescopic infrared spectroscopy (as reviewed in Esposito et al. (1997), Mills et al. (2007), and Titov et al. (2018)). Spectral measurements for vapor-phase H_2SO_4 include radio occultation (e.g., Imamura et al. (2017), Kolodner and Steffes (1998), and Oschlisniok et al. (2021)).

Several other species in the aerosols have also been proposed. While H_2O is among the presumed species (≤25% by mass), direct quantitative measurements for aerosol H_2O have not been previously indicated. Other proposed minor species include ferric (Fe^{3+}) chloride and/or ferric sulfates (e.g., Jiang et al. (2024); Krasnopolsky (2017); Markiewicz et al. (2014); and Petrova (2018)), condensed sulfur (Porshnev et al., 1987), and the tentative presence of bulk iron and phosphorus (Andreichikov et al., 1987; Petryanov et al., 1981a, 1981b). Nevertheless, these species have yet to be confirmed.

Here, we demonstrate that the LNMS data contain several mass signals, related to aerosol composition, which were misassigned or left uncharacterized in the original LNMS investigations. In Mogul, Limaye & Way (2023), we showed that the LNMS spectra from the sub-cloud atmosphere possess several unexplained spikes in the ion counts at differing mass positions. In post-flight PVLP studies (Fimmel, 1983; Seiff et al., 1995), a review of the LNMS housekeeping data (which monitored the instrument operations, but was not archived) revealed several unexplained spikes in the ion pump current in the sub-cloud atmosphere. These observations are significant since they serve as further evidence of the aerosol thermal decomposition and subsequent release of the decomposition products into the LNMS.

In this context, we re-analyzed and re-interpreted the LNMS data as the thermal and evolved gas analysis of aerosols possessing a heterogeneous chemical composition. In our approach, the altitude trends from the LNMS and the LGC were re-interpreted as thermal decomposition profiles that followed the temperature gradient of the PVLP descent (−30 to 462°C from ∼65 km to the surface, Seiff et al. (1985)). These interpretations of the LNMS and LGC results as evolved gas analyses are parallel to those conducted for the Sample Analysis at Mars (SAM) package on the Mars Curiosity rover (McAdam et al., 2014, 2022) and the Thermal and Evolved Gas Analyzer (TEGA) on the Mars Phoenix lander (Hoffman et al., 2008; Sutter et al., 2012).

In the following sections, we detail extraction of the chemical composition, weight percentage, and mass loading of the cloud aerosols. We describe the methods used to analyze the LNMS data, which were adapted from the procedures developed for the LNMS in Mogul et al. (2021), Mogul, Limaye & Way (2023), and Mogul, Avice, et al. (2023). To construct the thermal decomposition profiles from the LNMS data, the abundances of key gases (e.g., SO_2, H_2O, O_2, and SO_3) were expressed against the temperatures of the intake inlets—rather than altitude. The procedures used to extract the LNMS inlet temperatures and heating rates are described. We additionally provide the necessary context for re-evaluating the LNMS and LGC results by summarizing critical PVLP descent parameters, instrumental design specifications, and calibrations. Many of these instrumental specifications are currently unknown to the Venus community. This includes the design of the gas collection assemblies and inlet heating specifications, which are described in restricted PVLP project reports (controlled by the International Traffic in Arms Regulations; ITAR). Hence, these details will likely assist in the design of future atmospheric sampling instruments. The acronyms and parameters used in this report are summarized in Tables 1 and 2.

Table 1
List of Abbreviations in Alphabetical Order

GC	Gas Chromatograph
GSV	Gas Sample Valve Assembly
ITAR	International Traffic in Arms Regulations
ISAV 1 and 2	Vega 1 and 2 UV Spectrometers
LGC	Large Probe Gas Chromatograph
LIR	Large Probe Infrared Radiometer
LNMS	Large Probe Neutral Mass Spectrometer
LCPS	Large Probe Cloud Particle Size Spectrometer
NIR	Near Infrared Spectroscopy
OS	Optical Spectroscopy
PV	Pioneer Venus
PVLP	Pioneer Venus Large Probe
SAM	Sample Analysis at Mars; Mars Curiosity
TEGA	Thermal and Evolved Gas Analyzer; Mars Phoenix
UVS	Ultraviolet Spectrometer
V12	Venera 12
V13/14	Venera 13 and 14
V11/13/14/15	Venera 11, 13, 14, and 15

2. Data and Methods

2.1. Data, Project Reports, and Laboratory Notebooks for the PVLP

The availability of LNMS data, laboratory notebooks of J. H. Hoffman (Principal Investigator in the original LNMS project), and PVLP project reports used in this study are described in the Open Research section.

2.2. Summary of the PLVP Descent and Atmospheric Sampling Instruments

The PVLP descended through Venus' atmosphere and reached the surface (4.4°N, 304.0°) on the eastern side of Rhpisunt Mons near the equator on 9 December 1978 (Fimmel, 1983). The PVLP descent profile included parachute deployment at ∼66 km, release of the aeroshell at ∼65 km, and parachute jettison at ∼45 km (Large & Small Probe Data Book, 1976). As described in Seiff et al. (1982), Lorenz (2022), and Lorenz (2025), the dynamics of the PVLP descent were slightly unsteady with an angle of attack of ≤3° and pitch oscillations of ≤8°. The PVLP spin rate during the descent was 15 rpm (revolutions per minute) just after release from the PV Multiprobe (Large & Small Probe Data Book, 1976; Nothwang, 1980), ∼16 rpm at ∼65 km (Tomasko et al., 1980), and ∼6–10 rpm just before surface impact (Lorenz, 2022).

The PVLP instrument payload (Figure 1a) is described in Fimmel (1983). The LNMS and LGC (Table 1), instruments onboard the PVLP, yielded measurements of atmospheric composition during descent to the surface. Also considered in this study were the PVLP nephelometer, cloud particle size spectrometer (LCPS), and infrared radiometer (LIR) (Figure 1), which yielded data relating to the scattering coefficients for particles in the clouds, total aerosol mass loading, and sub-cloud water abundances.

The LNMS (Hoffman et al., 1979; Hoffman, Hodges, Wright, et al., 1980; Hoffman, Hodges, Donahue, & McElroy, 1980) was a single focusing, magnetic sector, and electron ionization mass spectrometer. The original LNMS mass scale (1–208 amu) was re-expressed in Mogul, Limaye & Way (2023) as 1–208 u (unified atomic mass unit) and interpreted as m/z 1–208 (m/z, mass to charge ratio) to account for double and triple charged species (e.g., $^{36}Ar^{2+}$, $^{136}Xe^{2+}$, and $^{136}Xe^{3+}$). Ion counts in the LNMS were measured at 232 pre-selected mass positions across the 1–208 u mass scale rather than at regular measurement intervals. This strategy permitted the acquisition of 232 high-resolution measurements (mass resolution of ∼0.001–0.01 u between 15 and 136 u) over a short period of 64 s per spectrum (Hoffman et al., 1979; Hoffman, Hodges, Wright, et al., 1980; Hoffman, Hodges, Donahue, & McElroy, 1980). The downside of this strategy was that several mass positions were only partly characterized, while other mass positions were skipped and not measured.

The LNMS data set includes 49 total mass spectra (Hoffman, 1978b). The LNMS data set includes (a) 4 background spectra obtained before opening of the inlets, (b) 38 complete spectra acquired at an electron ionization energy of 70 eV and obtained between 64.2 and 0.9 km, (c) 3 spectra acquired at 30 eV and obtained at 54.0, 30.1, and 9.1 km, (d) 3 spectra acquired at 22 eV and obtained at 52.7, 28.1, and 8.2 km, and (e) 1 partial spectrum obtained at 0.2 km (70 eV), which was interrupted at ∼34 u by surface impact. The LNMS data set also contains 1 incomplete spectrum from 56.8 km, which possessed no counts. Across the descent, the LNMS mass spectra were obtained at intervals of 2.3–1.0 km before parachute jettison (between the altitudes of 64.2–49.4 km) and at intervals of 3.2–0.7 km after parachute jettison (between the altitudes of 45.2–0.2 km).

The LGC was a gas chromatograph that contained two chromatographic columns, reference columns, and thermal conductivity detectors, which operated in parallel to separate the low- and high-boiling point samples from the atmosphere (Oyama, Carle, Woeller, Rocklin et al., 1980; Oyama, Carle, Woeller, Pollack et al., 1980). The LGC was designed similarly to the Viking Lander Gas Exchange Experiment (Oyama, Carle, Woeller, Pollack et al., 1980). The LGC analyzed atmospheric samples at the altitudes of 51.6, 41.7, and 21.6 km (Oyama, Carle, Woeller, Rocklin et al., 1980; Oyama, Carle, Woeller, Pollack et al., 1980).

Table 2
List and Description of Parameters Used in the Study

Δcounts	difference in ion counts using 24.4 km as a reference
i and j	target chemical species and species chosen for comparison
x, y, z	example species chosen for comparison
n_i	number density for species i from the atmosphere (number of molecules of i per volume)
N_i	number of molecules, or number abundances, of species i released from the captured aerosols
x_i	mixing ratio of species i
a	altitude
I_i	ion counts for species i
ρ_i	sensitivity factor for species i
v_i	transmission coefficient for species i
σ_i	electron ionization cross section for species i
f_i	fraction of the target ion for species i
MM_i	molecular mass for species i
T_D	temperature of maximum decomposition
$N_i^{\max}$	maximum number of released molecules of species i
σ_i^{stdev}	standard deviation for $N_i^{\max}$ (same units as $N_i^{\max}$)
N_i^T	total number of molecules of species i released from the captured aerosols
$N_{SO_2}^T$	total number of SO_2 molecules released from the captured aerosols
$N_{SO_2}^{H_2SO_4}$	number of SO_2 molecules released from H_2SO_4 decomposition
$N_{SO_2}^{MSO_4}$	number of SO_2 molecules released from metal sulfate decomposition
$N_{H_2O}^T$	total number of H_2O molecules released from the captured aerosols
$N_{H_2O}^{H_2SO_4}$	number of H_2O molecules released from H_2SO_4 decomposition
$N_{H_2O}^{\text{hydrates}}$	number of H_2O molecules released from the hydrates
$N_{H_2O}^{\text{soln}}$	number of H_2O molecules released from the aerosol solution phase
N_i^{aerosol}	number of molecules of species i in the aerosols
g_i	grams of species i
g_x, N_x	total grams and number of molecules of species x
g_y, N_y	total grams and number of molecules of species y
g_z, N_z	total grams and number of molecules of species z
wt%	weight percent
p_i^{app}	apparent partial pressure for species i
p_T	total atmospheric pressure
n_C^T	total number densities of CO_2 and N_2 in the aerosol collection column
mg m^{-3}	mg of sample per m^3 of the atmosphere

2.3. Altitude, Temperature, Pressure Scales

The altitude scales from the original LNMS, LGC, LCPS, PVLP nephelometer, and LIR investigations were retained in this study (see Table 1 for abbreviations) (Hoffman, Hodges, Donahue, & McElroy, 1980; Knollenberg & Hunten, 1980; Oyama, Carle, Woeller, Pollack et al., 1980; Ragent et al., 1985). The altitude scales for these instruments were based on data obtained by the Atmospheric Structure Investigation published in Seiff et al. (1980) and differ slightly (≤0.76 km) from the revised and accepted scale in Seiff et al. (1985). For the LGC, comparison of the reported pressure and altitude relationships in Oyama, Carle, Woeller, Pollack et al. (1980) to the relationships in Seiff et al. (1985) suggest that the LGC altitudes were slightly underestimated (by ∼1.7, 0.2, and 1 km at 51.6, 41.7, and 21.6 km, respectively). The altitude scales from the Venera 11–14 investigations were likely based on data from Venera 9 (Keldysh, 1977) and were overestimated by ∼1–3 km between ∼50 and 42 km when compared to the scales in Seiff et al. (1980, 1985). The altitude scales for the Vega 1 and 2 investigations were based on data in Linkin et al. (1986) and minimally differ from the scales in Seiff et al. (1980, 1985) (≤0.3 km and ≤0.9 km between ∼35 and 60 km, respectively). For the LNMS, the atmospheric temperatures at the altitudes of measurement were obtained by interpolating the PVLP temperature and altitude data in Seiff et al. (1985). To obtain estimates with <10% error, the data from Seiff et al. (1985) were separately interpolated between 0 and 50 km ($R^2 = 0.9999$) and 51–70 km ($R^2 = 0.9998$) using the 6th order polynomials in Table 3.

2.4. LNMS and LGC Gas Collection Assemblies

Relevant design parameters for the PVLP inlet assemblies were extracted from the following PVLP project reports: Large & Small Probe Data Book (1976), Final Report, Definition Phase Program of the Large Probe Neutral Mass Spectrometer for Pioneer Venus (1977), LNMS Final Project Report (1978), and Acceptance Test Report (1977). The LNMS and LGC sampled Venus' atmosphere using separate intake inlets, which were installed on opposing sides of the PVLP (Final Report, Large Probe Neutral Mass Spectrometer, 1978; Large & Small Probe Data Book, 1976). As outlined in Figure 1b, the LNMS and LGC inlets were located at 65 and 265°, with the atmospheric instrument pressure inlet positioned at 0°. The LNMS and LGC inlets protruded ∼1 cm from the PVLP surface and ∼0.64 cm outside the estimated spacecraft boundary layer or probe viscous flow region. This indicated that the LNMS and LGC inlets, by design, sampled the atmosphere on different sides of the PVLP and did not sample spacecraft outgassing (Final Report, Large Probe Neutral Mass Spectrometer, 1978; Large & Small Probe Data Book, 1976). Consequently, the LNMS and LGC inlets were subjected to a wide range of atmospheric temperatures throughout the PVLP descent.

The LNMS inlets were composed of tantalum (Hoffman et al., 1979; Hoffman, Hodges, Wright, et al., 1980; Hoffman, Hodges, Donahue, & McElroy, 1980) and passivated using sulfuric acid to yield an inner oxide layer (Book 2, part 2; page 45; Hoffman (1976-1979)). The tips of the LNMS inlets, which protruded into the atmosphere, were crimped to constrain the inner dimensions (≤100 nm inner gap), which restricted atmospheric intake (Final Report, Large Probe Neutral Mass Spectrometer, 1978; Large & Small Probe Data Book, 1976). The LNMS inlets opened to the atmosphere at ∼64 km through the explosive removal of a hermetically sealed cover (Hoffman et al., 1979; Hoffman, Hodges, Donahue, & McElroy, 1980; Hoffman, Hodges, Wright, et al., 1980). Atmospheric samples were actively

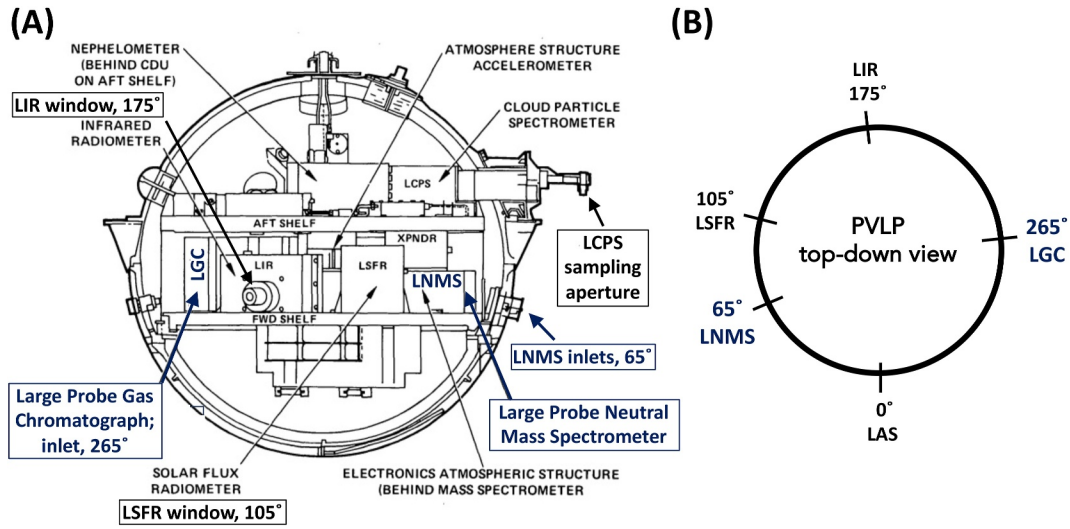

Figure 1. Diagrams of the Pioneer Venus Large Probe pressure vessel. (a) Side view showing the instrument arrangement (adapted from Panagakos & Waller (1978)). (b) Top-down view showing the positions of the inlets for the Large Probe Atmospheric Structure Experiment (LAS), Neutral Mass Spectrometer (Large Probe Neutral Mass Spectrometer), and Gas Chromatograph (Large Probe Gas Chromatograph), and windows for the Solar Flux Radiometer (LSFR) and Infrared Radiometer (LIR) (Large & Small Probe Data Book, 1976). Sampling aperture for the Large Probe Cloud Particle Size Spectrometer is shown in (a).

acquired through the LNMS inlets due to the low pressure in the ion source cavity ($\leq 10^{-8}$ bar), which was maintained through the use of chemical getters and ion pumps (Hoffman et al., 1979).

Per our understanding, the LGC inlet (160 mm, outer diameter; 159 mm, inner diameter) did not possess a sealed cover and was exposed to the atmosphere immediately after release of the PVLP aeroshell (Large & Small Probe Data Book, 1976; Oyama, Carle, Woeller, Pollack et al., 1980; Oyama, Carle, Woeller, Rocklin et al., 1980). Passive acquisition through the LGC inlet fed atmospheric samples into the Gas Sample Valve (GSV) assembly, which controlled gas temperatures and flow toward the chromatographic columns (Acceptance Test Report, 1977; Oyama, Carle, Woeller, Pollack et al., 1980; Oyama, Carle, Woeller, Rocklin et al., 1980). To prevent sample condensation after acquisition, the GSV was heated to 60, 130, and 160°C (Oyama, Carle, Woeller, Rocklin et al., 1980; Oyama, Carle, Woeller, Pollack et al., 1980) during the LGC measurement intervals at 51.6, 41.7, and 21.6 km (Oyama, Carle, Woeller, Pollack et al., 1980), respectively. The LGC heating steps matched the respective atmospheric temperatures (~60, 130, and 290°C) at the altitudes of measurement, barring the GSV temperature at 21.6 km (160°C), which remained under the reported temperature threshold for LGC integrity (≤180°C) (Oyama, Carle, Woeller, Rocklin et al., 1980). Ram pressures encountered during the descent potentially assisted sample acquisition through the LNMS and LGC inlets.

Table 3
List of Relevant Equations Used for Interpolation in the Study

Equations for interpolating the temperature versus altitude (km) data from Seiff et al. (1985).	
0–50 km	$T\,(°C) = -1.11776959082696 \times 10^{-7}x^6 + 1.47178885567811 \times 10^{-5}x^5 - 6.66604775659607 \times 10^{-4}x^4 + 1.21788942856256 \times 10^{-2}x^3 - 8.68984401968191 \times 10^{-2}x^2 - 7.51575320106349x + 4.6219306005456 \times 10^2$
51–70 km	$T\,(°C) = -2.07045167621711 \times 10^{-6}x^6 + 8.87319732964631 \times 10^{-4}x^5 - 1.55833799257801 \times 10^{-4}x^4 + 1.43807345087176 \times 101 \times^{3} - 7.36198812713354 \times 102 \times^{2} + 1.98284945516271 \times 10^4x - 2.19417856062175 \times 10^5$
Equation describing the LNMS inlet heating rate versus altitude (km) relationship after parachute jettison.	
43.5–0.2 km	$\text{Heat Rate}\ (°C\ min^{-1}) = -1.5423 \times 10^{-5}x^4 + 1.0314 \times 10^{-3}x^3 - 1.4129 \times 10^{-2}x^2 + 0.23159x + 4.8879$

2.5. Heating Profiles for the LNMS and LGC Inlets

The external inlets on the LNMS (Hoffman, Hodges, Wright, et al., 1980) and LGC (Oyama, Carle, Woeller, Rocklin et al., 1980) were heated during operation to prevent the condensation of atmospheric gases and collection of particles. According to our understanding of the LNMS project reports (Final Report, Definition Phase Program of the Large Probe Neutral Mass Spectrometer for Pioneer Venus, 1977; Final Report, Large Probe Neutral Mass Spectrometer, 1978), the LNMS inlets were heated by applying low power (≤0.5 W) to a variable pitch wire coiled around the inlets. According to the LNMS project reports (Final Report, Definition Phase Program of the Large Probe Neutral Mass Spectrometer for Pioneer Venus, 1977; Final Report, Large Probe Neutral Mass Spectrometer, 1978), this applied low power yielded temperatures of ∼25 to 10°C above atmospheric conditions before parachute jettison, and ∼5 to 2.5°C above atmospheric conditions after parachute jettison (∼45–3 km). In contrast, no power (or heat) was applied at < 2.5 km. According to our understanding of an LGC project report (Acceptance Test Report, 1977), the LGC inlet temperatures were regulated by external sensors at ≤6°C (51.7 km), 13°C (41.6 km), and 16°C (21.6 km) above the atmospheric temperatures.

For the LNMS, the magnitude of inlet overheating (Δ°C) was obtained by interpolating the calibration data extracted from the LNMS project reports (Final Report, Large Probe Neutral Mass Spectrometer, 1978). The atmospheric temperatures at the altitudes of the LNMS measurements were obtained as described in Section 2.3. The respective atmospheric temperatures were adjusted using the magnitude of overheat obtained from the interpolated calibration data. The total heating adjustments to the LNMS inlets translated to a temperature range of ∼−1 to 460°C across the LNMS sampling column (64.2–0.2 km) with the respective atmospheric temperatures being ∼−28 to 460°C. The rates of heating (°C min^{-1}) for the LNMS inlets were obtained using the timestamp and altitude profiles for the PLVP descent obtained from Seiff et al. (1980).

2.6. LNMS Data Analysis and Peak Fitting

The LNMS spectra obtained at the electron ionization energies of 70, 30, and 22 eV were independently treated using the peak-fitting, normalization, and unit conversion strategies described in Mogul et al. (2021), Mogul Limaye & Way (2023), and Mogul, Avice, et al. (2023). For chemical species represented by 1 mass measurement (e.g., SO_2^+ and SO_3^+), the mass point was tracked across all altitudes. For example, the vertical trends for SO_2 were obtained by tracking changes at the sole measurement at 63.960 u (a pre-selected mass position), while trends for SO_3 were obtained by tracking the changes at 79.958 u (a pre-selected mass position). For species represented by ≥ 2 mass points in the LNMS data (e.g., H_2O^+ and O_2^+), the respective peak profiles were fitted using Gauss functions. Expected peak shapes and mass errors were obtained using the in-flight behavior of the LNMS internal standards (CH_3^+, CO^+, N_2^+, $^{40}Ar^+$, and $^{136}Xe^+$), as detailed in Mogul, Limaye & Way (2023). Relevant isobars or species with overlapping masses (or *m*/*z* values) were considered.

For H_2O, peak fitting was conducted as described in Mogul, Limaye & Way (2023) and independently performed for each spectrum at the LNMS mass positions of 17.985, 18.010, and 18.034 u (referred to herein as 18 u). The peak fits at 18 u accounted for several isobaric species to H_2O, including $^{36}Ar^{2+}$, $^{18}O^+$, and potentially NH_4^+. As described in Mogul, Limaye & Way (2023), the peak fits were optimized by constraining the abundances for $^{18}O^+$ and $^{36}Ar^{2+}$ (isobars to H_2O) using the counts for $^{16}O^+$ and the LNMS isotope ratio for $^{18}O/^{16}O$, and the counts for $^{36}Ar^+$ and the LNMS ionization ratio for $^{40}Ar^{2+}/^{40}Ar^+$, respectively.

For O_2, peak fitting was conducted in each spectrum at the LNMS mass positions of 31.972 and 31.990 u (32 u). Peak fits at 32 u accounted for O_2^+ and isobaric $^{32}S^+$. Fitted counts for O_2^+ (70 eV) were corrected for contributions from CO_2 ionization, which yielded O_2^+ as a side product (Final Report, Definition Phase Program of the Large Probe Neutral Mass Spectrometer for Pioneer Venus, 1977; Monteiro-Carvalho et al., 2024). The O_2^+ arising from CO_2 ionization was estimated by (a) extracting the O_2^+/CO_2^+ ratio ($\sim 2 \times 10^{-4}$) from the lab-measured LNMS control spectra obtained at 100 eV (Final Report, Definition Phase Program of the Large Probe Neutral Mass Spectrometer for Pioneer Venus, 1977), (b) adjusting the O_2^+/CO_2^+ ratio from 100 eV by ∼50% to obtain the O_2^+/CO_2^+ ratio from 70 eV, consistent with the absolute cross sections for O_2^+ formation from CO_2 ionization, which decrease by ∼50% between ∼100 and 70 eV (Monteiro-Carvalho et al., 2024), and (c) calculating the expected counts for O_2^+ at each altitude by multiplying the respective counts of CO_2^+ by the O_2^+/CO_2^+ ratio from 70 eV ($\sim 1 \times 10^{-4}$). While the peak fits at 32 u were reasonable, disambiguation was likely incomplete given the limited data coverage (only 2 mass points). Control peak fitting for O_2^+ using the maximum and minimum peak widths and mass errors (Mogul, Limaye & Way, 2023) suggested uncertainties of ≤10%.

As determined in Mogul, Limaye & Way (2023), standard deviations for the LNMS counts were 3.6% for fitted species and species represented by a single mass point with counts of >600, and 14.2% for species represented by a single mass point with counts of <600. Instrument noise was considered negligible as indicated in calibration studies (Hoffman, Hodges, Wright, et al., 1980) and since counts of 0 were measured at multiple mass positions (>140 u) at various altitudes in the in-flight data.

2.7. Identifying the Aerosol Decomposition Products

The LNMS spectra were parsed for spikes (temporary increases in the ion counts) that occurred after aerosol collection beginning at ~51 km. These spikes were interpreted as signature gases and compounds that arose from the decomposing aerosols. For the data obtained after the clog (<25 km), the spikes were identified by following the change in counts (Δcounts) at each altitude, using 24.4 km as the reference altitude. This treatment allowed for a direct comparison across the 232 pre-selected LNMS mass positions at < 25 km, which exhibited a wide range in the ion counts (1–~2 × 10^6 counts). Chemical assignments for these spikes were predicated upon (a) measurement of ≥1 count at ≥3 consecutive altitudes in the descent profile, (b) sufficient overlap between the measured LNMS mass position/s and the target mass, which was assessed using the expected peak shapes and mass errors, as detailed in Mogul, Limaye & Way (2023), (c) consideration of potential isobars, and (d) precedence of the chemical species in the NIST database (Wallace, 2020) or literature. The chemical assignments (exact mass in parenthesis) at the respective LNMS mass positions were: H_2O^+ (18.011 u) at 18 u, fitted as described in Section 2.6; O_2 (31.990 u) at 32 u, fitted as described in Section 2.6; SO^+ (47.967 u) at 47.966 u, HSO^+ (48.975 u) at 48.974 u, $HSOH^+$ (49.983 u) at 49.968 u; SO_2 (63.962 u) at 63.960 u; FeO^+ (71.930 u) at 71.973 u; $SO_3{}^+$ (79.957 u) at 79.958 u; $HSO_3{}^+$ (80.965 u) at 80.847 u, $H_2SO_3{}^+$ (81.973 u) at 81.975 u; $H_2SO_4{}^+$ (97.968 u) at 97.948 u; $MgSO_4{}^+$ (119.937 u) at 119.981 u; $Na_2SO_4{}^+$ (141.932 u) at 141.882 u; $NiSO_4{}^+$ (153.887 u) at 153.894 u; $CoSO_4{}^+$ (154.885 u) at 154.911 u, and Mn_2O_3 (157.861 u) at 157.876 u.

2.8. Extracting the LNMS Number Densities, Number Abundances, and Mixing Ratios

The LNMS number densities (n), number of molecules (N), volume mixing ratios (x), and associated errors were extracted from the 70, 30, and 22 eV spectra using the procedures adapted from Mogul, Avice, et al. (2023), Donahue and Hodges (1992), and Hoffman, Hodges, Donahue, and McElroy (1980). Table 2 provides an explanation for the parameters used in this section. Number densities (n) refer to the number of atmospheric gas molecules acquired and measured by the LNMS (e.g., number of atmospheric molecules per cm^3). The number of molecules (N), or number abundances, refer to the number of gas molecules that were released from the captured aerosols in the inlets and measured by the LNMS (e.g., number of molecules released per total aerosol materials collected). The values for n and N were obtained by comparing the ionization, fragmentation, and transmission behavior of the target species to CO_2, the dominant gas in the LNMS data. Mixing ratios refer to the ratio of the target species expressed against CO_2 and N_2, the most abundant gases in Venus' atmosphere. This significantly updates the procedures for the LNMS from Donahue and Hodges (1992), which obtained number densities by comparison to $^{40}Ar^+$ and expressed mixing ratios solely against CO_2.

Through Equations 1A and 1B, ion counts (I_i) for the target species (i) were respectively converted to n_i or N_i (defined above and in Table 2) using a species-specific sensitivity factor (ρ_i). Through Equation 2, the species-specific ρ_i was related to the ratios of the transmission coefficients (v_i), cross sections (σ_i), fraction of the respective ions (f_i), and exact molecular mass (MM_i) between the target species and CO_2 (Mogul, Avice, et al., 2023). Through Equation 3, mixing ratios (x_i) at each altitude (a) for the target atmospheric gases were calculated using n_i and the summed number densities for CO_2 and N_2 ($I_{CO_2} + n_{N_2}$), followed by expression as ppm (10^{-6}) by volume. Apparent mixing ratios for the aerosol-derived gases were obtained by substituting N_i for n_i in Equation 3. Uncertainties from all terms were propagated. Electron ionization cross sections (σ) at 70, 30, and 22 eV were obtained from the NIST database (Kim et al., 2004) for SO_2, H_2O, and N_2, and literature sources for CO_2 (Straub, Lindsay et al., 1996) and O_2 (Straub, Renault et al., 1996). The σ for SO_3 (70 eV) was assumed to be equivalent to SO_2. Best fits to the data were obtained by assuming $a \pm 4$ eV uncertainty in the LNMS electron energies.

$$n_i = \rho_i I_i \tag{1A}$$

$$N_i = \rho_i I_i \tag{1B}$$

Table 4
The Parent Ion Fractions (f_i) for SO_2, H_2O, and CO_2 (at 70, 30, and 22 eV)

Parent ion	Energy	LNMS f	Reference f
SO_2^+	70 eV	0.62 ± 0.07	0.67[a], 0.58[b]
	30 eV	0.64 ± 0.02	0.61[b]
	22 eV	0.70 ± 0.01	0.75[b]
H_2O^+	70 eV	0.81 ± 0.02	0.82[a], 0.77[c]
	30 eV	0.88 ± 0.02	0.83[c]
	22 eV	0.97 ± 0.02	0.92[c]
CO_2^+	70 eV	0.73 ± 0.03	0.69[a], 0.71[d]
	30 eV	0.75 ± 0.06	0.88[d]
	22 eV	0.88 ± 0.06	0.95[d]

Note. Values from the LNMS, NIST, and literature sources were calculated using Equations 4–6. [a]NIST; Kim et al. (2004). [b]Basner et al. (1995). [c]Straub et al. (1998). [d]Straub, Lindsay et al. (1996).

$$\rho_i = \left(\frac{v_{CO_2}}{v_i}\right)\left(\frac{\sigma_{CO_2}}{\sigma_i}\right)\left(\frac{f_{CO_2}}{f_i}\right)\left(\frac{MW_{CO_2}}{MW_i}\right)^{1/2} \tag{2}$$

$$(x_i)_a = \left(\frac{n_i}{n_{CO_2} + n_{N_2}}\right)_a = \left(\frac{(I_i)\left(\frac{v_{CO_2}}{v_i}\right)\left(\frac{\sigma_{CO_2}}{\sigma_i}\right)\left(\frac{f_{CO_2}}{f_i}\right)\left(\frac{MW_{CO_2}}{MW_i}\right)^{1/2}}{I^a_{CO_2} + n^a_{N_2}}\right)_a \tag{3}$$

$$f_{SO_2} = \frac{SO_2^+}{(SO_2^+ + SO^+)} \tag{4}$$

$$f_{H_2O} = \frac{H_2O^+}{(H_2O^+ + OH^+)} \tag{5}$$

$$f_{CO_2} = \frac{CO_2^+}{\left(CO^{18}O^+ + {}^{13}CO_2^+ + CO_2^+ + C^{18}O^+ + {}^{13}CO^+ + CO^+ + O^+\right)} \tag{6}$$

Fractions of the parent ions (f_i) at 70, 30, and 22 eV were extracted from the LNMS mass data and calculated using Equations 4–6. Values for f_i from 70 eV were averaged and the error propagated across 29 spectra acquired in the sub-cloud atmosphere (<45 km). Values for f_i from 30 and 22 eV were averaged across the 3 respective spectra. Table 4 lists the f_i for SO_2^+, H_2O^+, and CO_2^+ from the LNMS (70, 30, and 22 eV), NIST, and comparable literature sources (Basner et al., 1995; Straub, Lindsay et al., 1996; Straub et al., 1998; Wallace, 2020), which were collectively calculated using Equations 4–6.

As adapted from Mogul, Avice, et al. (2023), the transmission coefficients (v_i) were obtained by interpolation of published data regarding the LNMS calibration standards (Donahue & Hodges, 1992). Ion transmission was assumed to be independent of ionization energy. Therefore, identical values for v_i were used for the 70, 30, and 22 eV spectral analyses. Values of v_i for H_2O (18 u) and N_2 (28 u) were obtained by interpolation using the linear relationship between v_i and mass of the LNMS calibration standards between 15 and 40 u (3 points, $R^2 = 0.9977$). Values of v_i for SO_2 (64 u) and CO_2 (44 u) were obtained by interpolation using the linear relationship between log (v_i) and log (mass) for the LNMS calibration standards between 20 and 131 u (3 points, $R^2 = 0.9984$). Standard errors of the regressions were propagated as the uncertainty for v_i. For data obtained during the clog (LNMS altitudes of 50.3–25.9 km) when atmospheric gas intake was limited, the mixing ratios were calculated using expected CO_2 abundances, which were estimated using calibration data from the original LNMS investigations (Hoffman et al., 1979) and the procedures described in Mogul, Limaye & Way (2023).

2.9. Constructing the LNMS Thermal Decomposition Profiles

The thermal decomposition profiles for the captured aerosols were constructed by plotting N_i for SO_2, H_2O, SO_3, and O_2 against the LNMS inlet temperatures at the measurement altitudes. The inlet temperatures were extracted from the LNMS project reports as described in Section 2.5. The peaks (or spikes) in the thermal profiles were fit to Gauss functions and the regressions minimized by least squares analysis (MS Excel, Solver), which yielded the temperatures at maximum decomposition (peak center; T_D, °C), maximum number of molecules released from the captured aerosols (peak height; N_i^{max}), and the associated standard deviation for N_i^{max} (peak width parameter; σ_i^{stdev}, same units as N_i^{max}). For H_2O, the inclusion of sequential and overlapping peaks yielded excellent approximations to the asymmetric release profile for H_2O from the aerosols. Fits to the data were sequentially conducted for each peak, in succeeding pairs of peaks, and across all peaks in the respective profiles. Equation 7 was used to calculate the peak areas (Dyson, 1998), which were defined as the total number of molecules released from the captured aerosols (N_i^{rel}).

$$N_i^{rel} = \frac{N_i^{max}\,\sigma_i^{stdev}}{0.3989} \tag{7}$$

2.10. Calculating the Abundances of the Aerosol Components

2.10.1. Reaction Pathways of Aerosol Decomposition

The thermal decomposition steps of the captured aerosols were characterized using Reactions 8–16. Reaction 8 summarizes the thermally unstable compounds that were present in the aerosols and/or formed within the LNMS inlet after capture. These compounds included H_2O, H_2SO_4, hydrated metal sulfates ($M_x(SO_4)_y{\cdot}nH_2O$), and uncharacterized hydrates ($X{\cdot}nH_2O$), where n = relative number of H_2O for each species. The thermal dehydration and decomposition of these species was assumed to proceed through a temperature-dependent and stepwise process, consistent with the literature studies on hydrated geological samples (e.g., Thomas et al. (2007), McAdam et al. (2014), and Kubliha et al. (2017)), hydrated metal sulfates (Frost et al., 2006; Majzlan et al., 2017; Spratt et al., 2014; Tagawa, 1984; Xu et al., 2010), and H_2SO_4 (Corgnale et al., 2020). Therefore, the thermal decomposition of the captured aerosols was assumed to include the temperature-dependent and stepwise loss of H_2O, decomposition of sulfate (from H_2SO_4 and metal sulfates), and formation of metal oxides (from the metal sulfates).

$$\text{aerosol} \rightarrow a\,H_2O + b\,H_2SO_4 + c\,M_x(SO_4)_y\cdot\,nH_2O + d\,X\,nH_2O \tag{8}$$

The thermal decomposition of H_2SO_4 and associated hydrates are described in Reactions 9–11. Reaction 9 describes the dehydration of hydrated H_2SO_4 ($H_2SO_4{\cdot}nH_2O$). Reactions 10 and 11 describe the stepwise structural decomposition of H_2SO_4 (Corgnale et al., 2020). The thermal dehydration and decomposition of hydrates of ferric sulfates are described in order across Reactions 12–14 and 11. Reactions 12 and 13 describe the dehydration of hydronium jarosite ($(H_3O)Fe_3(SO_4)_2(OH)_6$), an example hydrate of ferric sulfate. Reactions 14 and 11 describe the first and second decomposition steps for ferric sulfate ($Fe_2(SO_4)_3$), respectively (Frost et al., 2006; Majzlan et al., 2017; Spratt et al., 2014; Wu et al., 2013; Xu et al., 2010). Reaction 15 describes the thermal dehydration of other hydrated metal sulfates, such as sulfates of magnesium, sodium, and other metals. Reaction 16 describes the thermal dehydration of uncharacterized hydrates from the aerosols.

$$H_2SO_4\cdot nH_2O \rightarrow H_2SO_4 + n\,H_2O \tag{9}$$

$$H_2SO_4 \rightarrow SO_3 + H_2O \tag{10}$$

$$SO_3 \rightarrow SO_2 + 0.5\,O_2 \tag{11}$$

$$(H_3O)\,Fe_3(SO_4)_2(OH)_6 \rightarrow Fe_3(SO_4)_2(OH)_5 + 2\,H_2O \tag{12}$$

$$2\,Fe_3(SO_4)_2(OH)_5 \rightarrow 2\,Fe_3O_{2.5}(SO_4)_2 + 5\,H_2O \tag{13}$$

$$Fe_2(SO_4)_3 \rightarrow Fe_2O_3 + 3\,SO_3 \tag{14}$$

$$M_x(SO_4)_y \cdot nH_2O_n \rightarrow M_x(SO_4)_y + n\,H_2O \quad (15)$$

$$X \cdot nH_2O_n \rightarrow X + n\,H_2O \quad (16)$$

2.10.2. Calculating Aerosol Abundances of H_2SO_4, Ferric Sulfate, and Iron

The abundances of H_2SO_4, ferric sulfate, and iron in the aerosol phase were afforded using the mass balance relationship in Equation 17 and stoichiometric considerations in Reactions 10, 11, and 14. Table 2 explains the parameters used in this section. Equation 17 describes the total sources of the SO_2 that was released from the aerosols ($N^T_{SO_2}$) and measured by the LNMS. These total sources included (a) SO_2 released from H_2SO_4 ($N^{H_2SO_4}_{SO_2}$) (Reactions 10 and 11) and (b) SO_2 released from metal sulfates (MSO_4) that were thermally unstable ($N^{MSO_4}_{SO_2}$), which were presumed to be the ferric sulfates (Reactions 14 and 11).

$$N^T_{SO_2} = N^{H_2SO_4}_{SO_2} + N^{MSO_4}_{SO_2} \quad (17)$$

Therefore, consistent with Reactions 10 and 11, $N^{H_2SO_4}_{SO_2}$ was converted to the aerosol-phase abundances of H_2SO_4 ($N^{aerosol}_{H_2SO_4}$) using a 1:1 stoichiometry; where $N^{H_2SO_4}_{SO_2}$ related to the SO_2 released during the clog. Consistent with Reactions 14 and 11, $N^{MSO_4}_{SO_2}$ was converted to the aerosol-phase abundances of sulfate (SO_4^{2-}) arising from decomposed ferric sulfates ($N^{aerosol}_{SO_4}$) using a 1:1 stoichiometry; where $N^{MSO_4}_{SO_2}$ related to the SO_2 released after the clog at the higher temperatures. In turn, the $N^{aerosol}_{SO_4}$ was converted to the projected number of molecules of ferric sulfate ($N^{aerosol}_{Fe_2(SO_4)_3}$) and bulk iron ($N^{aerosol}_{Fe}$) in the aerosols using the stoichiometry of ferric sulfate ($1\,Fe_2(SO_4)_3 = 2\,Fe^{3+} + 3\,SO_4^{2-}$).

2.10.3. Calculating Aerosol Abundances of H_2O

Direct calculation of the total H_2O in the aerosol phase was obtained using the mass balance relationships in Equations 18–21, which described the release of H_2O from the aerosols. These calculations considered the stoichiometry of the thermal dehydration and decomposition reactions (Reaction 9–16). Table 2 explains the parameters used in this section. The total aerosol-phase H_2O ($N^{aerosol}_{H_2O}$) was defined in Equation 18 as the sum of the hydrate-phase H_2O ($N^{hydrates}_{H_2O}$) and solution-phase H_2O ($N^{soln}_{H_2O}$). In turn, Equation 19 was used to describe the total sources of the H_2O that was released from the aerosols $\left(N^T_{H_2O}\right)$ and measured by the LNMS ($N^T_{H_2O}$ = the total H_2O measured by the LNMS). These sources included (a) H_2O released from the structural decomposition of H_2SO_4 ($N^{H_2SO_4}_{H_2O}$) (Reaction 10), (b) hydrate-phase H_2O ($N^{hydrates}_{H_2O}$) released via the dehydration of hydrated H_2SO_4, hydrated and/or hydroxylated metal sulfates, and other hydrates (Reactions 9, 12–13, 15, and 16), and (c) minor abundances of H_2O released from the solution phase ($N^{soln}_{H_2O}$).

$$N^{aerosol}_{H_2O} = N^{hydrates}_{H_2O} + N^{soln}_{H_2O} \quad (18)$$

$$N^T_{H_2O} = N^{H_2SO_4}_{H_2O} + N^{hydrates}_{H_2O} + N^{soln}_{H_2O} \quad (19)$$

To properly account for $N^{H_2SO_4}_{H_2O}$ in Equation 19, we used the 1:1 stoichiometry from the decomposition of H_2SO_4 (Reactions 10 and 11) for the formation of H_2O ($N^{H_2SO_4}_{H_2O}$) and SO_2 ($N^{H_2SO_4}_{SO_2}$; from Equation 17). This step yielded the relationship of $N^{H_2SO_4}_{H_2O} = N^{H_2SO_4}_{SO_2}$. This relationship was substituted into Equation 19 to yield Equation 20. Substituting Equation 18 into Equation 20, followed by rearrangement, yielded Equation 21. The total aerosol-phase H_2O was thus directly calculated using Equation 21.

$$N^T_{H_2O} = N^{H_2SO_4}_{SO_2} + N^{hydrates}_{H_2O} + N^{soln}_{H_2O} \quad (20)$$

$$N^{aerosol}_{H_2O} = N^T_{H_2O} - N^{H_2SO_4}_{SO_2} \quad (21)$$

2.11. Calculating Relative Abundances in the Aerosols

Weight percent (wt%) was calculated using Equation 22 ($i = x$, y, or z = aerosol H_2O, H_2SO_4, or $Fe_2(SO_4)_3$, respectively; Table 2). Mole ratios were calculated using Equation 23 (i = target species, and j = species chosen for comparison; Table 2). The weight percent and mole ratios were separately calculated for the (a) parent aerosol species using the bulk aerosol abundances, (b) parent aerosol species that were released during the clog, and (c) parent aerosol species that were released after the clog. Due to the ratio-based calculations, the inclusion of the Avogadro constant (N_A) (as shown in Equations 22 and 23), total pressure, and temperature was unnecessary. Masses (g_i) for the parent aerosol species were obtained using the molecular masses (MM_i).

$$(wt\%)_i = \left(\frac{g_i}{g_x + g_y + g_z}\right) \times 100 = \left(\frac{\mathrm{MM}_i (N_i)/N_A}{\frac{(\mathrm{MM}_x) N_x + (\mathrm{MM}_y) N_y + (\mathrm{MM}_z) N_z}{N_A}}\right) \times 100 \tag{22}$$

$$(\text{mole ratio})_i = \left(\frac{\text{mol}_i}{\text{mol}_j}\right) = \left(\frac{N_i}{N_j}\right) = \left(\frac{N_i/N_A}{N_j/N_A}\right) \tag{23}$$

2.12. Calculating the Aerosol Mass Loading Values

Mass loading values (mass per m^3) were calculated using an aerosol collection column, which was treated as a cylinder with a diameter of 0.98 m and height of 2.6 km. The collection column diameter was defined as the outer dimensions of the PVLP (0.98 m) or the distance between the drag plates on the adapter ring on the spherical pressure vessel (Dutta et al., 2023; Large & Small Probe Data Book, 1976). The collection column height (2.6 km) was defined as the distance between the altitudes of 51.0 and 48.4 km, where most of the aerosols were collected, as discussed further in Section 3.2. Table 2 explains the parameters used in this section.

To account for pressure and temperature in the collection column, concentrations were obtained using the ideal gas law. The respective gaseous decomposition products (SO_2 and H_2O) were treated as proxies for the parent aerosol compounds. Through Equation 24, the apparent partial pressures (p_i^{app}) for SO_2 and H_2O were obtained by comparing the respective values for N_i to the total expected number densities for CO_2 and N_2 within the collection column (n_C^T) (Mogul, Limaye & Way, 2023) and the total pressure (p_T) at the altitude of interest, which was chosen as 51.0 km (the start of the aerosol collection column).

$$p_i^{\text{app}} = \left(N_i / n_C^T\right) p_T \tag{24}$$

To obtain n_C^T, we integrated the plot of temperature versus the number densities for atmospheric CO_2 and N_2. These steps included (a) plotting the respective atmospheric temperatures (~−10 to 90°C) against the summed LNMS number densities for CO_2 and N_2 between 59.9 and 48.4 km (which retained a relationship between temperature and gas abundance, like the thermal decomposition profiles from Section 2.9), (b) fitting the plot to a quadratic polynomial, and (c) integrating across 51.0–48.4 km (~70–90°C) to obtain n_C^T, or the area under the curve. The procedures described in Mogul, Limaye & Way (2023) were used to obtain the projected LNMS number densities for CO_2 during the initial equilibration of the LNMS after inlet opening (≥58 km) and during the clog (~50–48 km), since the respective counts for CO_2^+ were less than expected. Counts for N_2^+ were disambiguated at 28 u and converted to number densities as described previously (Mogul, Limaye & Way, 2023; Mogul, Avice et al., 2023).

The resultant p_i^{app} values for SO_2 and H_2O from these calculations were then converted to concentration (mol m^{-3}) via the ideal gas law using the volume of the collection column and temperature and pressure at 51.0 km (69°C; 0.93 bar; Seiff et al. (1985)). In turn, these concentrations were converted to mass loading values (mg m^{-3}) for aerosol H_2O, $Fe_2(SO_4)_3$, H_2SO_4, bulk SO_4^{2-}, and bulk Fe^{3+} using the stoichiometric relationships from Reactions 9–15 and the respective molecular masses.

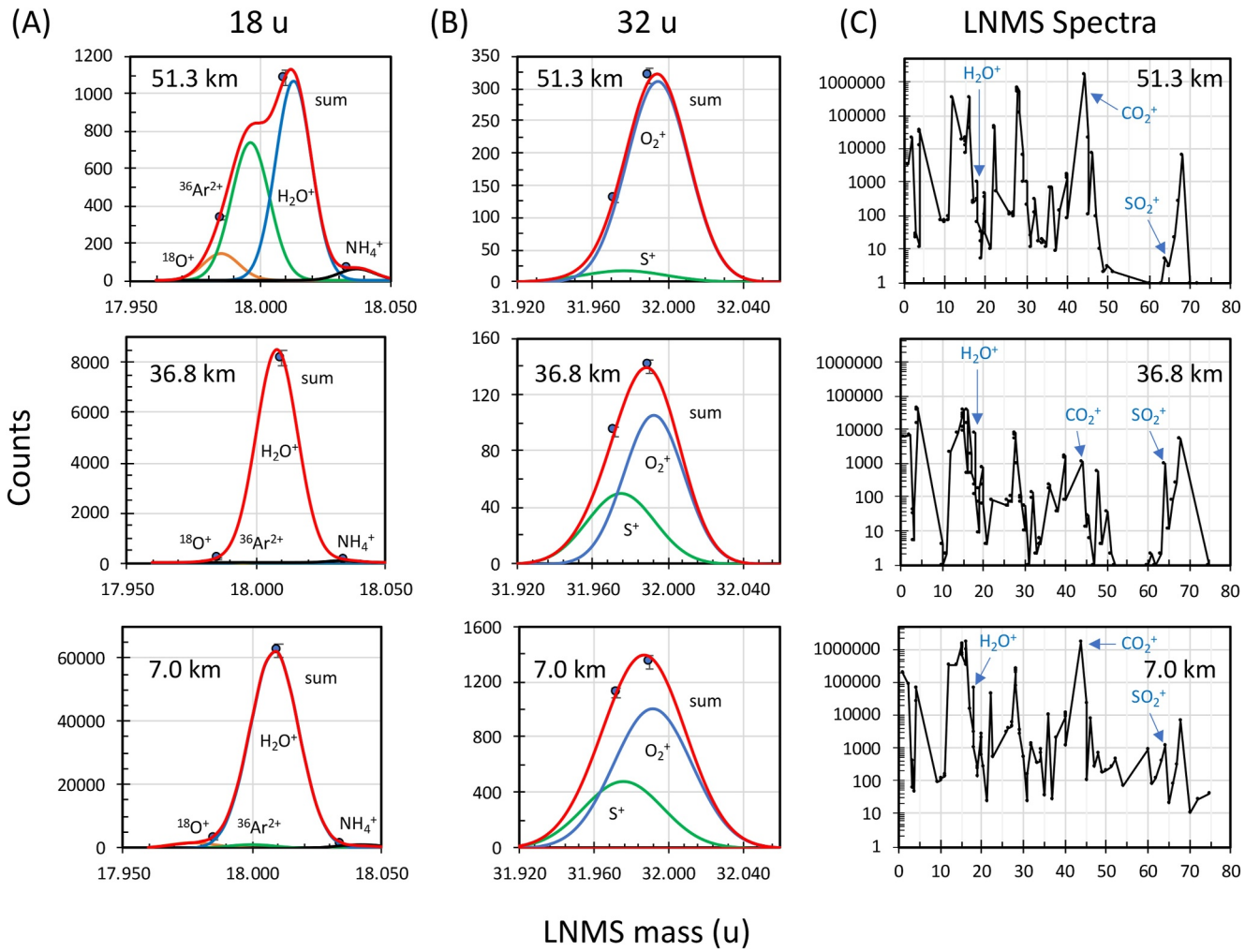

Figure 2. Peak fits and the Large Probe Neutral Mass Spectrometer (LNMS) spectra from before (51.3 km), during (36.8 km), and after the clog (7.0 km). (a) and (b) Respective peak fits at 18 u for H_2O^+ and 32 u for O_2^+ showing the included isobars and summed fit (red line). (c) The LNMS spectra from 1 to 75 u, where each respective mass position is connected by a black line and the change in measured counts for H_2O^+ (18 u), CO_2^+ (44 u), and SO_2^+ (64 u) are shown.

3. Results

3.1. Evidence for Nominal Behavior of the LNMS

The LNMS behavior during the descent was assessed by (a) comparing the fragmentation patterns for SO_2, CO_2, and H_2O from the 70, 30, and 22 eV spectra to published values (Table 4), (b) assessing the in-flight behavior of CO_2 and the internal standards, and (c) assessing the quality of the peak fits (Figure 2). All LNMS f_i values were consistent with the NIST database and/or literature values. The LNMS f_i values for SO_2^+ and CO_2^+ at 70 eV (Table 4) were within error to the NIST values (Kim et al., 2004). The LNMS f_i values for SO_2^+ and CO_2^+ at 70, 30, and 22 eV (Table 4) were within error to the literature values when considering the reported uncertainties in the cross sections for SO_2 (±15–20%; Basner et al. (1995)) and CO_2 (±3.5–7.5%, Straub, Lindsay et al. (1996)). The LNMS f_i value for H_2O^+ at 70 eV (Table 3) was consistent with the NIST value (Kim et al., 2004). The LNMS f_i values for H_2O^+ at 70, 30, and 22 eV, including the NIST value for H_2O^+ at 70 eV, was consistent with the literature values for D_2O^+ when considering the reported uncertainties (±4.5–5.5%; Straub et al. (1998)). However, the values from the LNMS (70, 30, and 22 eV; H_2O^+), NIST (70 eV; H_2O^+), and Straub et al. (1998) (70, 30, and 22 eV; D_2O^+) were higher than the values for H_2O^+ from Orient & Strivastava (1987), which suggested instrumental variances in the detection of OH^+ (per Equation 5).

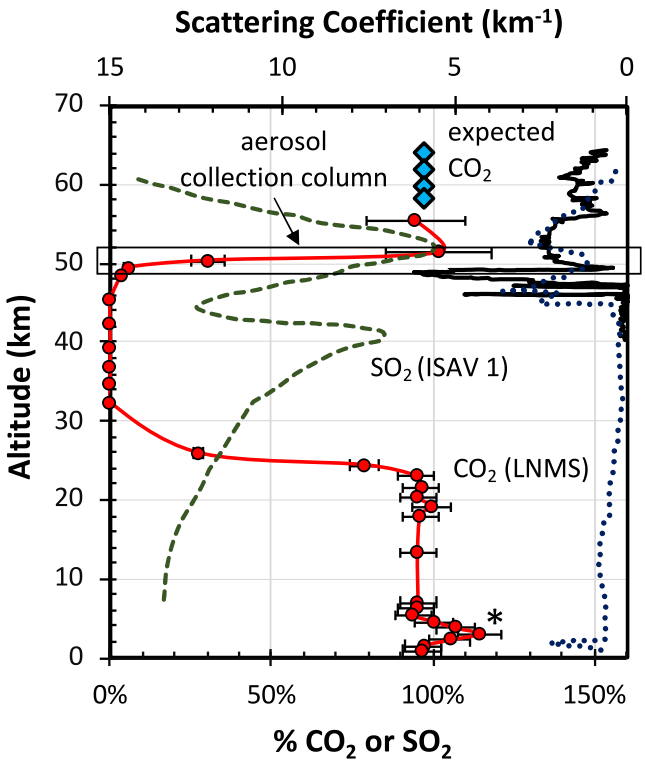

Figure 3. Impacts of aerosol collection on the CO_2 and SO_2 profiles from the Large Probe Neutral Mass Spectrometer (LNMS) and ISAV 1 (Vega 1) instruments. The aerosol collection column is highlighted at ~51–48 km (purple box). The lower *x*-axis represents the CO_2 densities (red circles and line) (Mogul, Limaye & Way, 2023) and SO_2 mixing ratios (green dashed line) (Bertaux et al., 1996), which are expressed as a percent of the Venus atmospheric densities and maximum reported mixing ratios, respectively; the blue diamond markers represent the expected Venus %CO_2, and the asterisk denotes the spike at 44 u in the LNMS data. The upper *x*-axis represents the particle scattering coefficients (right side of the plot) measured by the Pioneer Venus Large Probe (black line) and Venera 14 (blue dotted line) nephelometers.

We assessed the LNMS behavior during acquisition of the background and descent spectra using CO_2^+ and the LNMS internal standards (CH_3^+, CH_4^+, $^{40}Ar^+$, $^{40}Ar^{2+}$, $^{136}Xe^+$, $^{136}Xe^{2+}$, and $^{136}Xe^{3+}$). We tracked the changes in mass error, peak width, ionization yield, and fragmentation yield across all spectra (70 eV). Consistent with the analyses in Mogul, Limaye & Way (2023), the LNMS data (a) showed minimal changes in mass error and peak width for the LNMS internal standards, (b) the respective ionization yields were within expected ranges (e.g., $^{40}Ar^{2+}/^{40}Ar^+$, $^{136}Xe^{2+}/^{136}Xe^+$, $^{136}Xe^{3+}/^{136}Xe^+$), and (c) fragmentation yields were consistent with the NIST and/or MassBank EU databases (e.g., CO_2 and CH_4 fragmentation). The LNMS internal standards did not exhibit spikes in the ion counts during and after the clog (~50–25 km and <25 km, respectively), unlike the trends observed for SO_2, H_2O, O_2, SO_3, and other mass signals. These combined observations indicated the nominal behavior of the LNMS mass analyzer during all components of the PVLP descent with respect to ionization, fragmentation, and transmission.

Peak fitting at 18 and 32 u provided an assessment of the mass analyzer behavior. The LNMS peak fits were obtained by extracting the expected peak widths and mass errors using the in-flight behavior of the internal standards. Shown in Figures 2a and 2b are the example peak fits for H_2O and O_2 at 51.6 km (before the clog), 34.5 km (during the clog), and 7.0 km (after the clog). These peak fits showed excellent matches to the data, which indicated nominal ionization and transmission before, during, and after the clog. For comparison purposes, Figure 2c shows the full LNMS spectra (between 1 and 75 u) from 51.6, 34.5, and 7.0 km. These spectra highlight the respective changes for SO_2^+, H_2O^+, and CO_2^+ that occurred due to aerosol capture.

3.2. Aerosol Collection by the LNMS

We estimated the respective altitudes of major aerosol collection and inlet clogging by tracking the change in LNMS CO_2 densities across the descent (Mogul, Limaye & Way, 2023). As shown in Figure 3, the LNMS data yielded the expected CO_2 densities in the clouds between 55.4 and 51.3 km and deep lower atmosphere between 24.4 and 0.9 km. However, between these altitude ranges at 50.3–25.9 km, the LNMS CO_2 densities were ≤6,000−fold lower than expected. This significant but temporary decrease in CO_2 was attributed to aerosol capture, clogging of the inlets, reduction of atmospheric intake, and eventual resumption of nominal intake (Hoffman, Hodges, Donahue, & McElroy, 1980; Mogul, Limaye & Way, 2023). The loss in CO_2 is also evident in the unprocessed LNMS spectra in Figure 2c, which show the substantial loss and resumption in CO_2 counts during and after the clog, respectively. In Figure 3, the LNMS CO_2 densities are plotted against the particle scattering coefficients measured by the PVLP (Ragent et al., 1985) and Venera (Grieger et al., 2004) nephelometers. This comparison shows that the LNMS inlets clogged where particle scattering coefficients were the highest in the clouds, consistent with the proposed aerosol capture.

The aerosol collection column was thus identified by treating the LNMS CO_2 density profile as a proxy for aerosol collection and inlet clogging. The LNMS CO_2 densities, which were nominal at 51.3 km, decreased by ~70% and ≥95% in the succeeding measurements at 50.3 and 48.4 km, respectively. Hence, the aerosol collection column was defined as 51.0 to 48.4 km (highlighted box, Figure 3), or where most of the aerosols were captured during the descent, and most of the atmospheric intake had decreased. The volume of the collection column was defined as the volume displaced by the PVLP. Hence, the diameter of the collection column was defined as the outer dimensions of the PVLP (Section 2.12). Under this assumption, the PVLP inlets (Figure 1; Section 2.4) sampled on the perimeter of the collection column as gases were displaced around the descending, rapidly spinning, and slightly wobbling probe (e.g., unsteady angle of attack and pitch; Section 2.2 and references therein). Through the collection column, the PLVP descent time (3.0 min), fall speed (~13–16 m s^{-1}; Section 3.5.1), and spin rate (~6–13 spins km^{-1}) translated to ~15–36 total spins, or one spin every ~5–12 s (~5–12

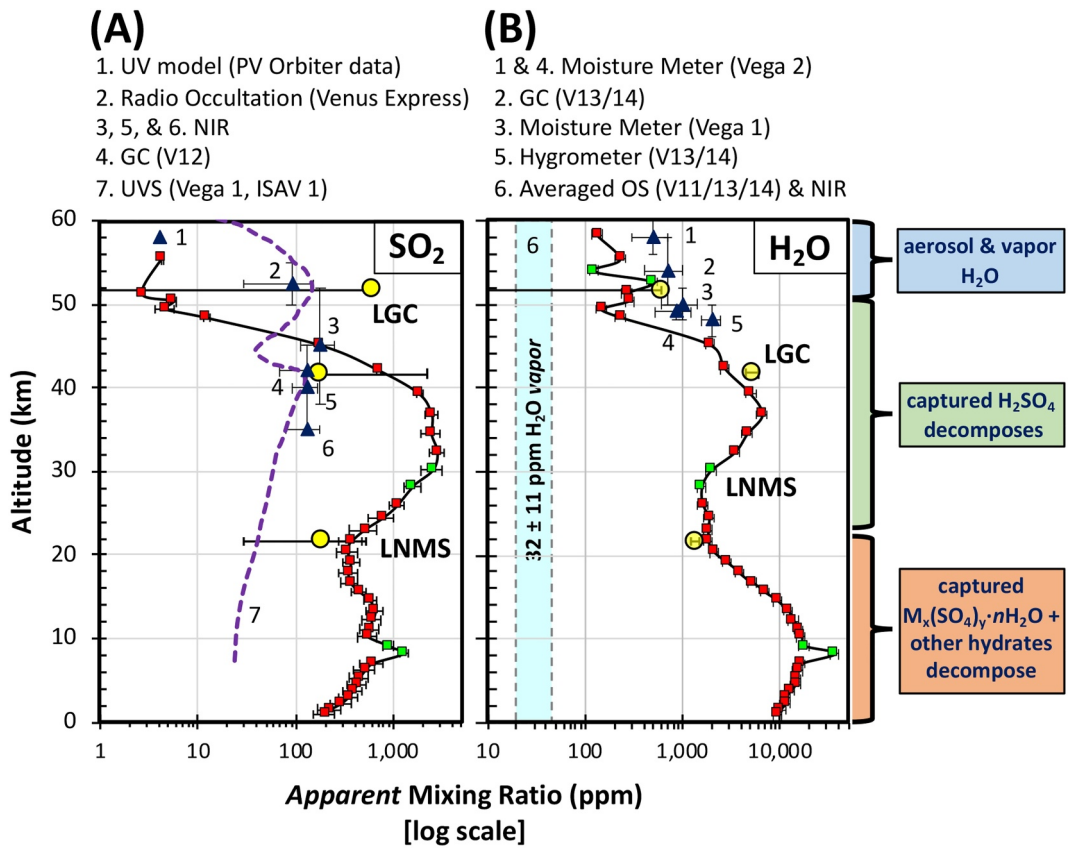

Figure 4. The Large Probe Neutral Mass Spectrometer (LNMS) apparent mixing ratios for (a) SO_2 and (b) H_2O compared to the Large Probe Gas Chromatograph (LGC) and other measurements. Brackets to the right of the plots indicate where the LNMS measured vapor and aerosol H_2O before aerosol capture and where SO_2 and H_2O were released from the aerosols during the thermal decomposition of H_2SO_4 (blue) and hydrated metal sulfates ($M_x(SO_4)_y{\cdot}nH_2O$) and other hydrates (red). The LNMS values (squares) were from the spectra obtained at 70 eV (red squares) and 30 and 22 eV (green squares). The LNMS error bars represent the propagated error. For the LGC (yellow circles), the error bars represent the reported 3 σ confidence intervals. The comparative Venus mixing ratios (blue triangles) for (a) SO_2 and (b) H_2O are listed in the legends. The abbreviations include GC (gas chromatograph), NIR (near infrared spectroscopy), OS (Optical Spectroscopy), UVS (UV spectroscopy), V12 (Venera 12), V13/14 (Venera 13 and 14), and V11/13/14 (Venera 11, 13, and 14).

rpm) (Lorenz, 2022; Seiff et al., 1980). These descent dynamics suggested sufficient sampling by the PVLP instruments to yield the representative concentrations of atmospheric gases and aerosols in the collection column.

As referred to herein, these assessments are consistent with a descent sequence that included the inadvertent collection of clog-inducing aerosols between 51.0 and 48.4 km, reduction of mass flow into the LNMS mass analyzer (e.g., atmospheric CO_2 and N_2) between ~50 and 25 km, and resumption of nominal intake after aerosol decomposition at <25 km (Hoffman, Hodges, Donahue, & McElroy, 1980; Mogul, Limaye & Way, 2023).

3.3. LNMS Altitude Profile for SO_2

In Figure 4a and Table 5, the apparent mixing ratios for SO_2 (xSO_2) from the LNMS and LGC are listed and compared to other Venus values. Congruent trends for the apparent xSO_2 are observed between the LNMS spectra obtained at 70, 30, and 22 eV, which was not indicated in the original LNMS investigations. Figure 4a shows that the LNMS xSO_2 substantially increased after aerosol collection (e.g., during and after the clog); congruent trends for the ion counts were observed in the unprocessed LNMS spectra in Figure 2c. To provide relevant context, the LNMS results were compared to the xSO_2 obtained by modeling of the ultraviolet spectroscopic measurements (UV) from the PV Orbiter (Winick & Stewart, 1980) (measurement 1 in Figure 4a), radio occultation from the Venus Express orbiter (Oschlisniok et al., 2021) (measurement 2 in Figure 4a), nightside orbital and telescopic near infrared spectroscopy (NIR) (measurements 3, 5, and 6 in Figure 4a) (Bézard & de Bergh, 2007; Marcq

Table 5
The SO_2 Mixing Ratios From the LNMS, LGC, and Other Venus Values

SO_2	Mixing ratios (ppm) at differing altitudes				
in situ analysis	~52 km	~42 km	~35 km	~22 km	~12 km
LNMS, PVLP[a]	3 ± 1 (51.3 km)	700 ± 150 (42.2 km)	2,500 ± 500 (36.8 km)	390 ± 80 (21.6 km)	640 ± 130 (12.2 km)
LGC, PVLP[b] [error: 1 σ; 3 σ]	<600 (51.6 km)	$176^{+296;\,2000}_{-0;\,0}$ (41.7 km)	–	$185^{+43;\,350}_{-43;\,155}$ (21.6 km)	–
GC, Venera 12[c]	–	130 ± 35 (≤42 km)	–	–	–
ISAV 1 and 2, Vega 1–2[d] (averaged)	108 ± 60	133 ± 11	–	38 ± 0	23 ± 4
remote analysis	~52 km	~42 km	~35 km	~22 km	~12 km
Chemical model, pioneer Venus orbiter data[e]	~4 (58 km)				
VeRa, Venus express[f]	90 ± 60 (52 ± 2 km)	–	–	–	–
VIRITIS-H, Venus express[g,h]	–	–	130 ± 50 (35 km) 190 ± 34 (35 ± 5 km)	–	–
NIR night spectra, Canada-France-Hawaii Telescope[i]	–	130 ± 40 (40 ± 5 km)	–	–	–
NIR night spectra, Canada-France-Hawaii telescope[j]	180 ± 70 (45 ± 7 km)	–	–	–	–

[a]Re-analyzed LNMS data. [b]Oyama, Carle, Woeller, Pollack et al. (1980). [c]Gel'man et al. (1980). [d]Bertaux et al. (1996). [e]Winick & Stewart (1980). [f]Oschlisniok et al. (2021). [g]Marcq et al. (2023). [h]Marcq et al. (2008). [i]Bézard et al. (1993). [j]Pollack et al. (1993).

et al., 2008; Marcq et al., 2023; Pollack et al., 1993), gas chromatography (GC) on Venera 12 (V12) (Gel'man et al., 1980) (measurement 4 in Figure 4a), and in situ ultraviolet spectroscopy (UVS) on Vega 1 and 2 (ISAV 1 and 2) (Bertaux et al., 1996) (measurement 7 in Figure 4a).

The LNMS altitude profile for $x SO_2$ exhibits minima at 51.3 km (3 ± 1 ppm) and 55.4 km (4 ± 1 ppm) (Figure 4a). These minima in LNMS $x SO_2$ were obtained during nominal intake and before aerosol capture. Hence, the LNMS $x SO_2$ at 51.3 and 55.4 km (~2–5 ppm, 51.3–55.4 km) likely represent the abundances of atmospheric SO_2 gas. In Winick & Stewart (1980), a similar $x SO_2$ (~4 ppm; 58 km) was obtained using photochemical models based on cloud top data for SO_2 obtained by the PV Orbiter (PVO) Ultraviolet Spectrometer. However, when considered together, the PVLP (LNMS) and PVO-based $x SO_2$ (Table 5) are ~36 and 30-fold lower than values obtained by Vega 1 and 2 (UVS) and Venus Express (radio occultation), respectively (Bertaux et al., 1996; Oschlisniok et al., 2021). These comparisons suggest considerable variability in atmospheric SO_2 in the clouds.

After aerosol capture, the LNMS profile for $x SO_2$ exhibits two maxima at ~32 km (2,800 ± 600 ppm) and ~10 km (550 ± 110 ppm) (Figure 4a). These LNMS $x SO_2$ are remarkably higher than all comparative Venus measurements (except the LGC). At ~42 km (Table 5), the LNMS $x SO_2$ (700 ± 150 ppm) is ~7−fold higher than values obtained by UVS on Vega 1 and 2, GC on V12, and NIR (Bertaux et al., 1996; Bézard et al., 1993; Gel'man et al., 1980). Yet, the LNMS and LGC values at ~42 km are within error (Table 5), when considering the broad and asymmetrical LGC errors reported as 1 and 3 σ (Oyama, Carle & Woeller, 1980, Oyama, Carle, Woeller, Pollack et al., 1980)—which likely represent the broad and asymmetric peak shapes observed for SO_2 in the LGC data (Oyama, Carle, Woeller, Pollack et al., 1980). In contrast, the LGC $x SO_2$ at ~42 km (Oyama, Carle & Woeller, 1980) is within error of the upper ranges of the other comparative measurements (Table 5).

Similarly, at ~35 km (Table 5), the LNMS $x SO_2$ (2,500 ± 700 ppm, 36.8 km) is ~14–19-fold higher than the values obtained via NIR from Venus Express (Marcq et al., 2008, 2023) ground telescopes (Pollack et al., 1993), and other studies (Arney et al., 2014; Bézard et al., 1993; Marcq et al., 2021). At ~22 km (Table 5), the LNMS

Table 6
The H_2O Mixing Ratios From the LNMS, LGC, and Other Venus Values

H_2O	Mixing ratios (ppm) at differing altitudes				
Direct analysis	~52 km	~42 km	~35 km	~22 km	~12 km
LNMS, PVLP[a]	270 ± 30 (51.3 km)	2,700 ± 290 (42.2 km)	6,600 ± 700 (36.8 km)	1,900 ± 200 (21.6 km)	14,000 ± 1,500 (12.2 km)
LGC, PVLP[b] [error: 1 σ and 3 σ]	<600 (51.6 km)	$5190^{+80;\,680}_{-80;\,680}$ (41.7 km)	–	$1350^{+20;\,150}_{-20;\,150}$ (21.6 km)	–
GC, Venera 13/14[c]	700 ± 300 (54 ± 4 km)	–	–	–	–
GC, Venera 12[d]	–	<100 ppm (≤42 km)	–	–	–
Hygrometer, Venera 13/14[e]	2,000 ± 400 (48 ± 2 km)	–	–	–	–
Moisture meter, Vega 1[f]	1,000 ± 400 (50 ± 2 km)	–	140 ± 60 (48–32 km)	–	–
Moisture meter, Vega 2[f]	850 ± 340 (49 ± 1 km)	–	120 ± 50 (31–30 km)	–	–
Indirect analysis	~52 km	~42 km	~35 km	~22 km	~12 km
OS, Venera 11, 13, 14[g]	30–40 (54 km)	20–40 (43–40 km)	23–30 (30 km)	20–30 (20–19 km)	18–70 (≤12 km)
VIRITIS-H, Venus Express[h]	–	–	31 ± 2 (40–30 km)	–	–
NIR Night Spectra, Apache Point Observatory[i]	–	34 ± 2 (45–20 km)	–	33 ± 2 (30–10 km)	29 ± 2 (≤15 km)
NIR Night Spectra, Canada-France-Hawaii Telescope[j]	–	30 ± 6 (47–23 km)	30 ± 7.5 (34–14 km)	–	30 ± 6 (47–3 km)

[a]Re-analyzed LNMS data. [b]Oyama, Carle, Woeller, Pollack et al. (1980). [c]Mukhin et al. (1982). [d]Gel'man et al. (1980). [e]Surkov et al. (1982). [f]Surkov, Shcheglov et al. (1986). [g]Ignatiev et al. (1997). [h]Marcq et al. (2008). [i]Arney et al. (2014). [j]Pollack et al. (1993).

xSO_2 (390 ± 80 ppm, 21.6 km) is well within error to the LGC measurement (Oyama, Carle & Woeller, 1980) when considering the reported 3 σ error. However, the LNMS and LGC xSO_2 at ~22 km are respectively ~10 and 5-fold higher than the values obtained by UVS on Vega 1 and 2 (Bertaux et al., 1996). Likewise, at ~12 km (Table 5), the LNMS xSO_2 is ~28−fold higher than the values obtained by UVS (Bertaux et al., 1996).

3.4. LNMS Altitude Profile for H_2O

In Figures 4b and Table 6, the apparent mixing ratios for H_2O (xH_2O) from the LNMS and LGC are listed and compared to other Venus values. Congruent trends for the apparent xH_2O are observed across the LNMS spectra obtained at 70, 30, and 22 eV, which was not indicated in the original LNMS investigations. Figure 4b shows that the LNMS xH_2O substantially increased after aerosol capture (e.g., during and after the clog); congruent trends for the ion counts were observed in the unprocessed LNMS spectra in Figure 2c. To provide relevant context, the LNMS results were compared to the selected xH_2O obtained by (a) direct and destructive analysis of atmospheric samples collected by the moisture meters on Vega 1 and 2 (Surkov, Shcheglov et al., 1986) (measurements 1, 3, and 4 in Figure 4b), GC on Venera 13 and 14 (V13/14) (measurement 2 in Figure 4b), hygrometers on V13/14 (Surkov et al., 1982) (measurement 5 in Figure 4b), and (b) indirect and non-destructive analysis of the atmosphere by in situ optical spectroscopy (OS) on Venera 11, 13, and 14, and 15 (V11/13/14/15) (Ignatiev et al., 1997, 1999) and orbital and telescopic nightside NIR (e.g., Arney et al. (2014); Marcq et al. (2008); Pollack et al. (1993)) (measurement 6 in Figure 4b, as averaged from Table 6).

Prior to aerosol capture (>51.0 km), the LNMS data yield xH_2O (~100–500 ppm, 51.3–59.9 km) that are ~3–16-fold higher than the values obtained by the listed spectroscopic measurements in Table 6 (32 ± 11 ppm H_2O;

averaged value from Table 6), including the OS measurements reported in Ignatiev et al. (1999). Yet, the LNMS $x\mathrm{H_2O}$ at ~52 km (e.g., 270 ± 30 ppm, Table 6) is within error limits to the broad measurements from the LGC (Oyama, Carle, Woeller, Pollack et al., 1980) and ~3–7-fold lower than values obtained by the GC on V13/14 (Mukhin et al., 1982), hygrometer on V13/14 (Surkov et al., 1982)), and moisture meters on Vega 1 and 2 (Surkov, Shcheglov et al., 1986).

After aerosol capture (<51.0), the LNMS altitude profile for $x\mathrm{H_2O}$ (Figures 4b, Table 6) exhibits two maxima at ~37 km (6,500 ± 700 ppm) and ~10 km (16,500 ± 1,800 ppm). These LNMS maxima in $x\mathrm{H_2O}$ are extraordinarily high when compared to the spectroscopic values listed in Table 6 (~200 and 515-fold higher, respectively), including the NIR measurements from ~35 km (~28–34 ppm) reported in Haus et al. (2015). The LNMS maxima are also much higher than values obtained by the GC on V12 (~65 and 165-fold higher, respectively), which began sampling below the cloud deck at ≤ 42 km, as understood from Gel'man et al. (1980). However, the LNMS and LGC $x\mathrm{H_2O}$ are similar at ~42–35 and ~22 km (Table 6). We also note that the LNMS and LGC values (~22 km) are roughly comparable to the tentative $x\mathrm{H_2O}$ (>500 ppm, <45 km) measured by the LIR (Revercomb et al., 1985). The comparable results between the LNMS, LGC, and LIR suggest aerosol deposition on the LIR window (Figure 1).

3.5. Thermal Decomposition Profiles From the LNMS Data

We treated the spikes for $\mathrm{SO_2}$, $\mathrm{H_2O}$, and other compounds in the LNMS data as products that evolved during the thermal dehydration and decomposition of aerosols captured from the clouds—and not as altitude trends for atmospheric gases. Parsing of the LNMS data also revealed spikes at masses consistent with $\mathrm{SO_3}$, $\mathrm{O_2}$, $\mathrm{H_xSO_y}$ (x = 0–2, y = 1–4), and differing metal-bearing species (e.g., $\mathrm{M_x(SO_4)_y}$ and $\mathrm{M_xO_y}$; M = metal). To demonstrate the temperature-dependent evolution of these gases and compounds, we extracted the estimated LNMS inlet temperatures at the altitudes of measurement (Section 2.5), including the inlet heating rates across the descent (Figure 5). Thermal profiles were then constructed by plotting the number of molecules (y-axis), or number abundances, for these released gases and compounds (from the 70, 30, and 22 eV spectra) against the LNMS inlet temperatures (x-axis) (Figures 6–11). The resultant peaks (or spikes) in the thermal profiles were fitted to multiple Gauss functions. As demonstrated in Figures 6–9, the inclusion of multiple overlapping peaks yielded excellent matches to the evolution profiles.

3.5.1. Heating of the LNMS Inlets During the Descent

The estimated range in LNMS inlet temperatures, LNMS inlet heating rates (Figure 5a), PVLP fall speed (Figure 5b), and PVLP acceleration (Figure 5c) were calculated using calibration information from the LNMS project reports (Final Report, Definition Phase Program of the Large Probe Neutral Mass Spectrometer for Pioneer Venus, 1977; Final Report, Large Probe Neutral Mass Spectrometer, 1978) and the PVLP descent profile (Seiff et al., 1980). The aerosol collection column at ~51–48 km is demarked as an oval in Figure 5a. After aerosol capture, the LNMS inlet temperatures ranged from ~80 to 460°C (~51–0.2 km), while the respective range in atmospheric temperatures was ~70–460°C. Heating rates for the LNMS inlets throughout the descent (Figure 5a) ranged from ~5 to 19°C $\mathrm{min^{-1}}$, which is comparable to the heating rates used in evolved gas analyses in laboratory studies (5–20°C $\mathrm{min^{-1}}$) and on Mars (35°C $\mathrm{min^{-1}}$) (Frost et al., 2006; McAdam et al., 2014; Spratt et al., 2014).

The LNMS inlet heating rates were dependent on the PVLP fall speed and acceleration (Figures 5b and 5c) and varied substantially before and after parachute jettison (demarked as the vertical dotted lines in Figure 5). The LNMS inlet heating rates after aerosol capture included (a) ~7.2 min at ~5°C $\mathrm{min^{-1}}$ (between ~51.2 and 45.1 km), (b) a rapid increase to ~19°C $\mathrm{min^{-1}}$ over ~0.2 min (between ~45.1 and 44.7 km) after jettison of the parachute, (c) ~0.3 min at ~19°C $\mathrm{min^{-1}}$ (between ~44.7 and 43.5 km), and (d) a steady, non-linear decrease from ~19 to 5°C $\mathrm{min^{-1}}$ over ~40 min (across ~43.5–0.2 km), as the PVLP descended through the dense lower atmosphere. The final decrease from ~19 to 5°C $\mathrm{min^{-1}}$ followed the 4th order polynomial (R^2 = 0.9991) provided in Table 3.

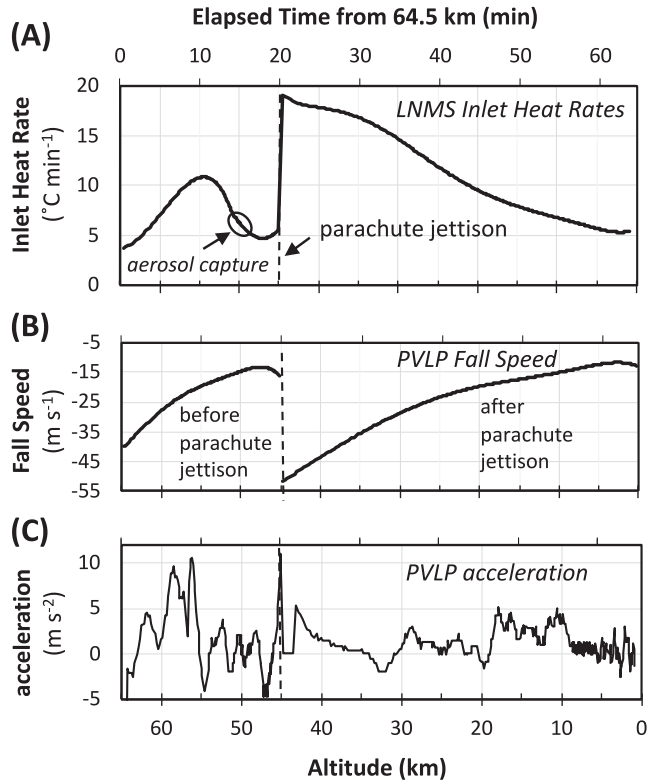

Figure 5. Profiles for the (a) Large Probe Neutral Mass Spectrometer inlet heat rate, (b) Pioneer Venus Large Probe (PVLP) fall speed, and (c) PVLP acceleration. Lower *x*-axis represents altitude (km); upper *x*-axis represents the elapsed flight time (minutes) beginning at ~64.5 km.

3.5.2. LNMS Thermal Profiles for Evolved SO_2 and H_2O

Figures 6–8 show the temperature-dependent, stepwise, and differential evolution of SO_2 and H_2O from the captured aerosols. These results were interpreted as the aerosols containing different compounds that decomposed in a temperature-dependent manner. This interpretation is consistent with the evolved gas and mass spectral analysis of Martian samples conducted by SAM and TEGA (McAdam et al., 2014, 2022; Sutter et al., 2012, 2024). Figure 6 shows that the maximal release of SO_2 from the captured aerosols occurred at 215 and 397°C, which is consistent with the release of SO_2 from ≥2 thermally unstable sulfate species. The release of SO_2 likely occurred during the decomposition of H_2SO_4 at 215°C (peak 1, Figure 6) and ferric sulfates at 397°C (peak 2, Figure 6), as justified in the following sub-sections.

Figures 7 and 8 show that the maximal release of H_2O from the captured aerosols occurred at 185 and 414°C, with several minor release steps at 35, 80, 118, 242, and 276°C. Peak ratios between H_2O and SO_2 increased by ~10-fold between 185 and 414°C, which is consistent with the dehydration or decomposition of more thermally stable compounds at the higher temperatures. These results are consistent with the stepwise dehydration and decomposition of several species, as described in Section 2.10.1.

Thus, the H_2O peaks in Figures 7 and 8 were respectively assigned to: (a) atmospheric water vapor and/or evaporative dehydration of non-clog-inducing aerosols (peak 1; 35°C), (b) dehydration of solution-phase H_2O from clog-inducing aerosols (peak 2; 80°C), (c) dehydration of slightly more thermally stable species like sulfuric acid hydrate ($H_2SO_4 \cdot nH_2O$; Reaction 9) and hydrated metal sulfates (e.g., $M_x(SO_4)_y \cdot nH_2O$; Reaction 15) (peaks 3 and 4; 118 and 185°C), (d) decomposition of H_2SO_4 (Reaction 10) and dehydration of other moderately thermally stable species, such as metal sulfates at differing hydration states (e.g., Reaction 15 for $M_x(SO_4)_y \cdot mH_2O$, where $m < n$) (peak 4; 185°C), (e) dehydration of intermediate hydrates formed after loss of H_2SO_4 and/or uncharacterized hydrates (e.g., Reaction 16) (peaks 5 and 6; 242 and 276°C), and (f) dehydration of more thermally stable

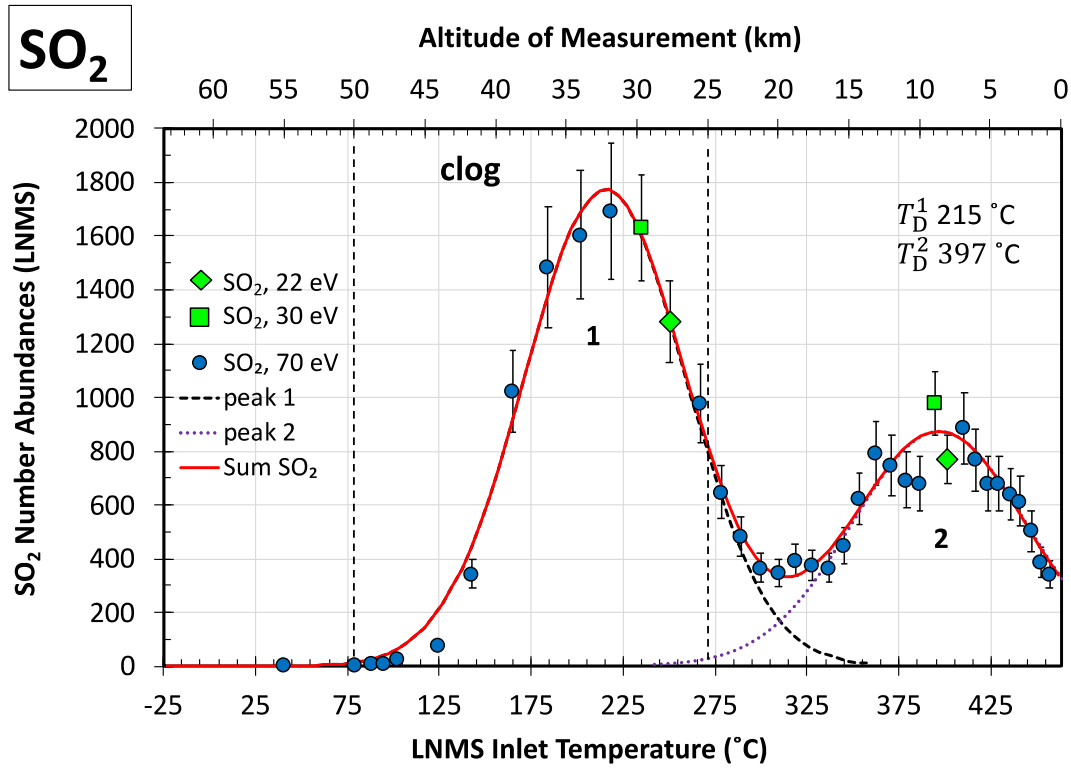

Figure 6. The Large Probe Neutral Mass Spectrometer (LNMS) evolved gas profile for SO_2 plotted against the LNMS inlet temperatures (lower *x*-axis) and altitudes of measurement (upper *x*-axis). Number abundances were extracted from the mass spectra obtained at 70 (circles), 30 (squares), and 22 eV (diamonds). Fits to the LNMS data (solid red lines) represent the sum of the numbered Gauss peaks (dashed and dotted peaks). Temperatures at maximum decomposition (T_D^n) for each peak (n) are listed. Propagated errors are displayed. Vertical dotted lines demark the LNMS clog (~50–25 km).

compounds like hydrated ferric and magnesium sulfates and other uncharacterized hydrates (e.g., Reactions 12, 13, 15, and 16) (peak 7; 414°C).

The LNMS H_2O thermal profile is expanded in Figure 8 to highlight peaks 1–6. This expanded view more clearly shows the H_2O measured before the clog (peak 1), H_2O released immediately after aerosol capture (peaks 2–6), and H_2O released from H_2SO_4 decomposition (peak 4). Figure 8 also compares the H_2O thermal profile with the cloud particle scattering coefficients measured by the PVLP and V14 nephelometers (Grieger et al., 2004; Ragent et al., 1985). The respective H_2O peaks measured before and during the clog (peaks 1–4; ~55–36 km) generally tracked with the increases in scattering coefficients at ~57–51 km (~2 km^{-1}) and ~50–45 km (~3–5 km^{-1}).

3.5.3. LNMS Thermal Profiles for Evolved SO_3, O_2, and H_xSO_y

Figure 9 compares the temperature-dependent evolution of SO_3, O_2, and SO_2 from the captured aerosols. Maximal release of SO_3 was tracked with SO_2 at 397°C (Figure 9). The number abundance for SO_3 was <5% of the value for SO_2, consistent with the limited detection of SO_3 observed in the original LNMS control studies (Hoffman, Hodges, Donahue, & McElroy, 1980). Maximal release of O_2 (peaks 3 and 6; Figure 9) at 205 and 392°C tracked with SO_2 (at 210 and 395°C, respectively). The number abundances for O_2 at 205 and 392°C were respectively ~3 and 51% of the values for SO_2. Because the expected value is 50% (Reaction 11), these trends suggest >95% losses of O_2 during the clog and negligible losses of O_2 below ~24 km. The observed release steps of O_2 at 7, 66, 273, 315, and 456°C (peaks 1, 2, 4, 5, and 7) suggest different sources for O_2 in the LNMS (Figure 9).

Figure 10 compares the temperature-dependent evolution of the different $H_xSO_y^+$ species ($x = 0–2$, $y = 1–4$) from the captured aerosols. Several spikes for $H_xSO_y^+$ were observed after the clog at ≥275°C (Figure 10). Trace spikes (≤20 counts) were observed for $H_2SO_4^+$, $H_2SO_3^+$, and HSO_3^+ across ~330–360°C, which generally

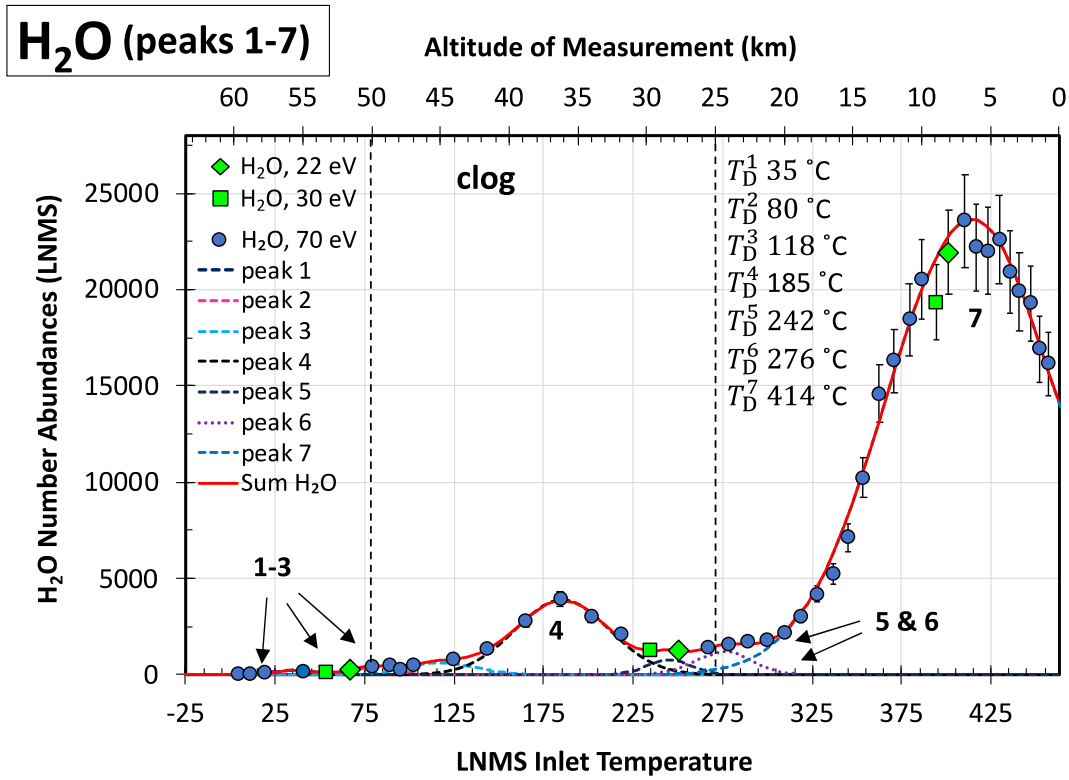

Figure 7. The Large Probe Neutral Mass Spectrometer (LNMS) evolved gas profile for H_2O (peaks 1–7) plotted against the LNMS inlet temperatures (lower *x*-axis) and altitudes of measurement (upper *x*-axis). Number abundances were extracted from the LNMS spectra obtained at 70 (circles), 30 (squares), and 22 eV (diamonds). Fits to the LNMS data (solid red lines) represent the sum of the numbered Gauss peaks (dashed and dotted peaks). Temperatures at maximum decomposition (T_D^n) for each peak (n) are listed. Propagated errors are displayed. Vertical dotted lines demark the LNMS clog (~50–25 km).

tracked with SO_2^+, SO^+, and SO_3^+ (Figure 10a). In contrast, high counts (Figure 10b) were observed for $HSOH^+$ (≤1,000 counts) and HSO^+ (≤350 counts). Potential isobars to the varying $H_xSO_y^+$ species include the phosphorus-bearing analogs ($H_{x+1}PO_y^+$), which are listed in the legends in Figure 10.

3.5.4. LNMS Thermal Profiles for Evolved Metal-Bearing Species

Parsing of the LNMS data revealed multiple spikes after the clog at masses relating to differing metal-bearing compounds (Figure 11). The LNMS data (Figure 11a) suggested the detection of FeO^+ (≤50 counts) across ~300–460°C (LNMS inlet temperatures). Consistent with literature studies, FeO^+ is assigned as a product of the electron ionization and fragmentation of Fe_2O_3 in the LNMS (Li et al., 2009; Yan et al., 2010), while Fe_2O_3 is assigned as a thermal decomposition product of $Fe_2(SO_4)_3$ (Reaction 14) (Frost et al., 2006; Majzlan et al., 2017; Spratt et al., 2014; Wu et al., 2013; Xu et al., 2010). The LNMS data (Figure 11b) also suggested the detection of other parent metal sulfates (≤5 counts). Potential intermittent release of sodium sulfate ($Na_2SO_4^+$) occurred at ≥280°C. The possible release of magnesium, nickel, and cobalt sulfate ($MgSO_4^+$, $NiSO_4^+$, and $CoSO_4^+$) occurred at ≥385°C. The possible detection of $Mn_2O_3^+$ occurred at ≥385°C. These results are congruent with literature studies, which show the low thermal stability of ferric sulfates compared to other metal sulfates (e.g., Mg, Ni, Co, and Mn), with respect to the release of SO_2 (Majzlan et al., 2017; Mu & Perlmutter, 1981; Spratt et al., 2014; Tagawa, 1984; Xu et al., 2010). Current efforts are focused on obtaining the number abundances for these species by extracting cross sections from the literature, if available.

3.6. LNMS Aerosol Composition

Weight percentage, mole ratios, and mass loading for the aerosol components are listed in Table 7. These values were obtained using the respective peak areas for SO_2 and H_2O from the thermal decomposition profiles (Figures 6–8) and the stoichiometric relationships outlined in Reactions 9–16 (Section 2.10). The decomposition

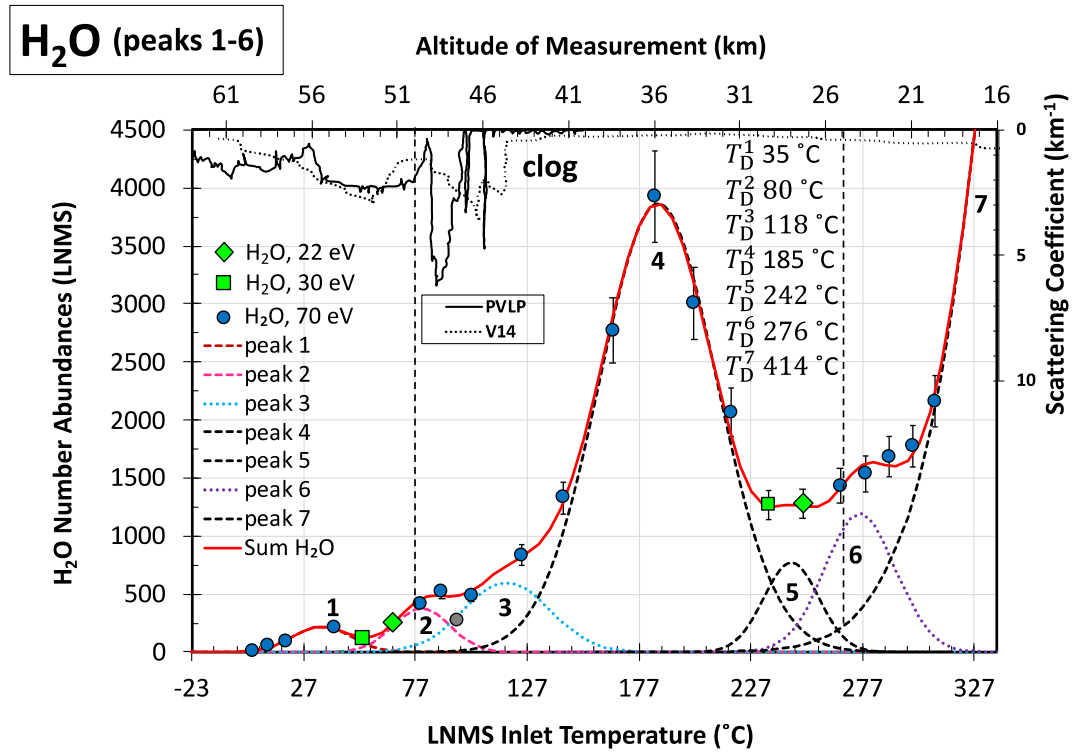

Figure 8. The expanded Large Probe Neutral Mass Spectrometer (LNMS) evolved gas profile for H_2O (showing peaks 1–6) plotted against the LNMS inlet temperatures (lower *x*-axis), altitudes of measurement (upper *x*-axis), and particle scattering coefficients (upper traces; right-side *y*-axis) measured by Pioneer Venus Large Probe and Venera 14 (V14). Number abundances were extracted from the LNMS spectra obtained at 70 (circles), 30 (squares), and 22 eV (diamonds). Fits to the LNMS data (solid red lines) represent the sum of the numbered Gauss peaks (dashed and dotted peaks). Temperatures at maximum decomposition (T_D^n) for each peak (n) are listed. Propagated errors are displayed. Vertical dotted lines demark the LNMS clog (~50–25 km).

yields were inferred to be high, given the Gauss-like distribution of the evolved gases (Figures 6–9). The total number abundance for H_2O ($N^T_{H_2O}$) was corrected for the H_2O released during H_2SO_4 decomposition (Equations 17–20), as described in Section 2.10.3. This correction enabled the extraction of aerosol H_2O (Equation 21). Due to the detection of FeO^+ after the clog, ferric sulfate ($Fe_2(SO_4)_3$) was assigned as the major source of SO_2 at the higher temperatures (peak 2, 397°C; Figure 6).

Accordingly, the inferred aerosol relative abundances were 62 ± 8 wt% aerosol H_2O, 16 ± 3 wt% $Fe_2(SO_4)_3$ (projected), and 22 ± 4 wt% H_2SO_4 (Table 7). Given the potential presence of other aerosol species that did not decompose and release signature gases, these values represented maximum percentages. The H_2O released from the captured aerosols (Table 7) was assigned as hydrate-phase H_2O released between ~270 and 460°C (59 ± 8 wt%), minor amounts of H_2O released from intermediate hydrates (3 ± 1 wt%) between ~80 and 270°C, and trace amounts of H_2O released from the solution phase (0.2 ± 0.1 wt%) between ~50 and 80°C. The bulk mole ratios in the aerosols were 87 ± 16 for $H_2O/Fe_2(SO_4)_3$, 15 ± 3 for H_2O/H_2SO_4, and 5.6 ± 1.1 for $H_2SO_4/Fe_2(SO_4)_3$.

The corresponding aerosol mass loading values were 4.2 ± 0.4 mg m^{-3} H_2O, 1.1 ± 0.1 mg m^{-3} $Fe_2(SO_4)_3$ (projected), and 1.5 ± 0.2 mg m^{-3} H_2SO_4 (Table 7). Additional mass loading values were 2.2 ± 0.2 mg m^{-3} for the bulk sulfate (SO_4) arising from all thermally unstable sulfate-bearing species, 0.3 ± 0.1 mg m^{-3} for projected Fe^{3+}, and 6.8 ± 0.5 mg m^{-3} for the total aerosol mass loading.

Gases released during the clog (~50–25 km; ~89–267°C) were independently treated and interpreted as the decomposition products that evolved from the volatile and thermally unstable components of the aerosols, such as H_2SO_4, intermediate hydrates, and solution-phase H_2O. Assessment of the evolved gases at ~50–25 km yielded the relative abundances of 86 ± 17 wt% H_2SO_4 and 14 ± 4 wt% H_2O (Table 7). The 14 ± 4 wt% H_2O was apportioned as 13.0 ± 4.0% H_2O released from intermediate hydrates (peaks 3–6, Figures 7 and 8) and 1.0 ± 0.1

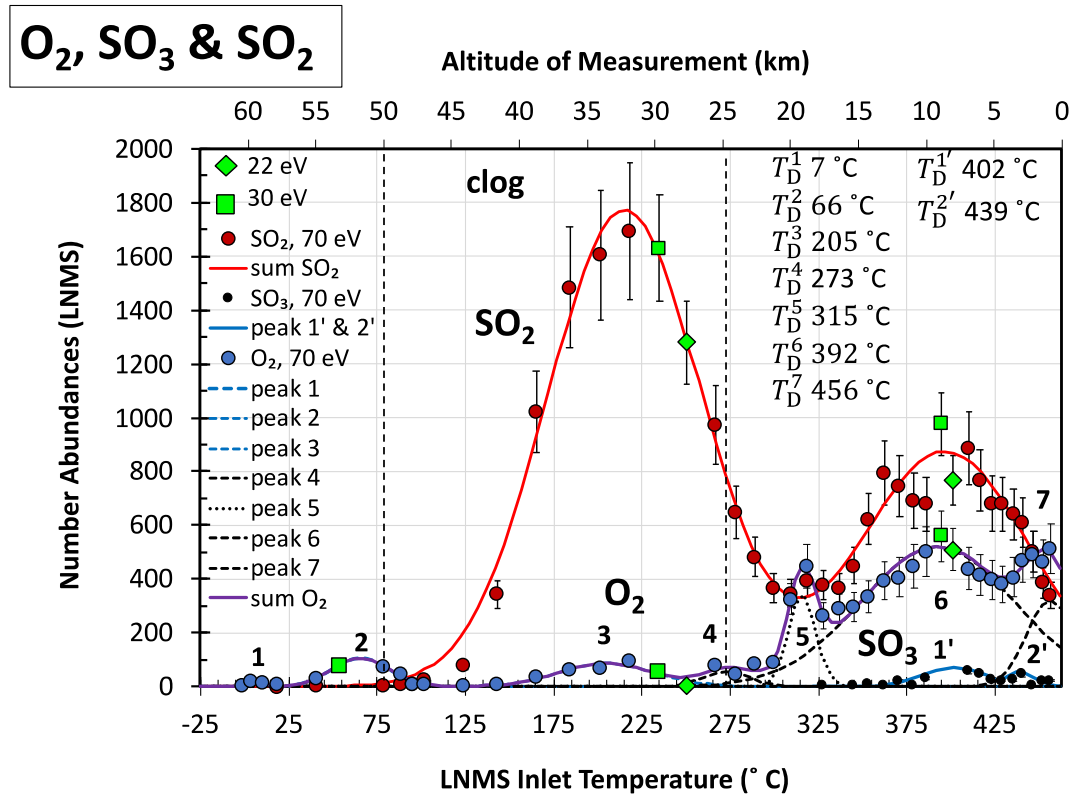

Figure 9. The Large Probe Neutral Mass Spectrometer (LNMS) evolved gas profiles for O_2 and SO_3 compared to SO_2 and plotted against the LNMS inlet temperatures (lower *x*-axis) and altitudes of measurement (upper *x*-axis). Number abundances were extracted from the 70 (circles), 30 (squares), and 22 eV (diamonds) spectra. Fits to the data (solid red lines) represent the sum of the numbered Gauss peaks (dashed and dotted peaks). Temperatures at maximum decomposition (T_D^n) for each peak (n) are listed. Propagated errors are displayed. Vertical dotted lines demark the LNMS clog (~50–25 km).

wt% from the solution phase. The corresponding mole ratio for H_2O/H_2SO_4 from gases released during the clog was 0.9 ± 0.2.

Gases released after the clog (<25 km; >267°C) were independently treated and interpreted as the decomposition products that evolved from less volatile and more thermally stable components of the aerosols, such as hydrated ferric sulfate and other hydrates. Assessment of the evolved gases at <25 km yielded 21 ± 3 wt% $Fe_2(SO_4)_3$ (projected) and 79 ± 12 wt% hydrate-phase H_2O. These values were obtained using peak 2 for SO_2 in Figure 6 and peak 7 for H_2O in Figure 7, respectively. The mole ratio for $H_2O/Fe_2(SO_4)_3$ from gases released after the clog was 82 ± 15.

3.7. LNMS Mixing Ratios for O_2

The xO_2 from the LNMS data were extracted at ~52 and 42 km to permit comparison to the published LGC values. LGC xO_2 was reported in Oyama et al. (1979a), corrected and left unconstrained in Oyama et al. (1980a), and subsequently updated in Oyama, Carle, Woeller, Pollack et al. (1980). The xO_2 from ~52 to 42 km from the LNMS (49 ± 6 ppm, 51.3 km; 19 ± 2 ppm, 42.2 km) are within error of the LGC xO_2 (43.6 ± 2.9 ppm, 51.6 km; 16 ± 1 ppm, 41.7 km) (Oyama, Carle, Woeller, Pollack et al., 1980). These results reveal good consistency between the two separate measurements of O_2 from the PVLP. LGC xO_2 from the deep and dense lower atmosphere (21.6 km) was not reported due to significant co-elution and peak overlap with N_2 (Oyama, Carle, Woeller, Pollack et al., 1980). At 52 km, the congruent LNMS and LGC xO_2 were obtained before aerosol capture (or the LNMS clog) and suggest that the middle clouds possess atmospheric O_2 and/or unidentified and non-clog inducing atmospheric compounds that released O_2 immediately after collection. At ~42 km, the congruent LNMS and LGC xO_2 (apparent), which were obtained after aerosol capture (and during the LNMS clog), suggest that

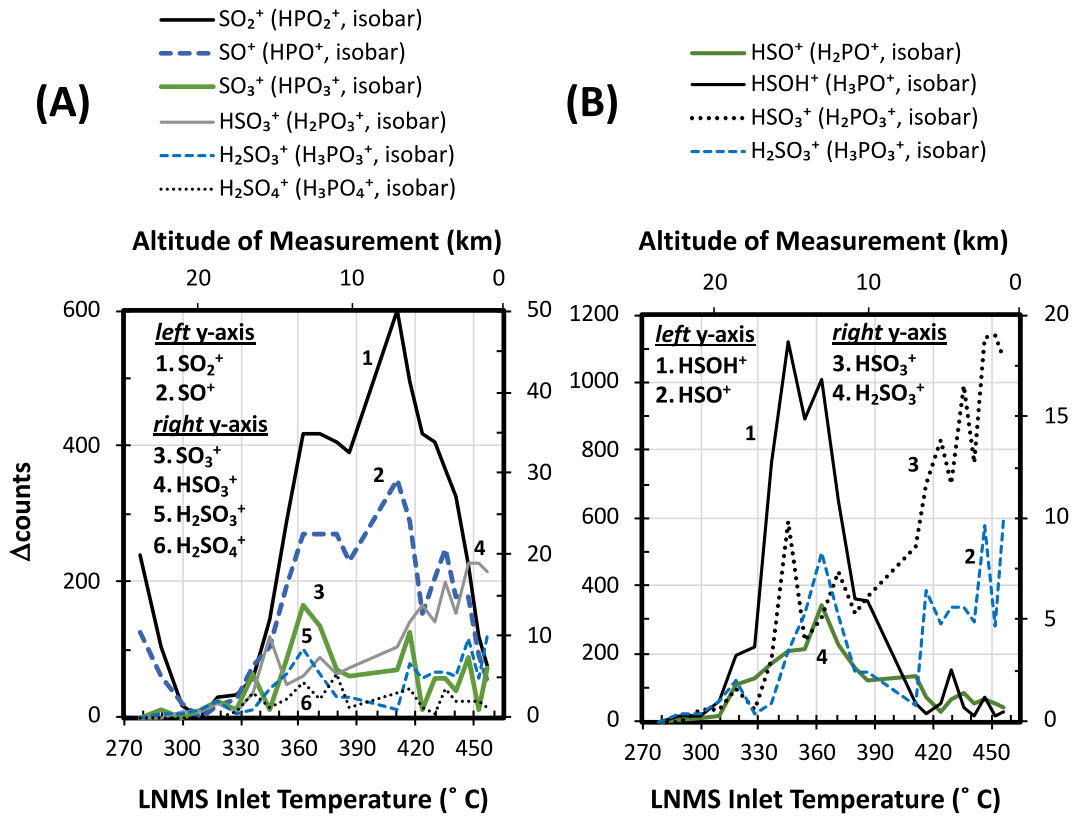

Figure 10. The Large Probe Neutral Mass Spectrometer (LNMS) evolved profiles for (a) SO_2^+, SO^+, SO_3^+, HSO_3^+, $H_2SO_3^+$, and $H_2SO_4^+$ and (b) $HSOH^+$, HSO^+, HSO_3^+, and $H_2SO_3^+$, where the change in counts (Δcounts), using 24.4 km as the reference, are plotted against the LNMS inlet temperatures (lower *x*-axis) and altitude of measurement (upper *x*-axis). Phosphorus isobars for H_xSO_y are provided in the legends.

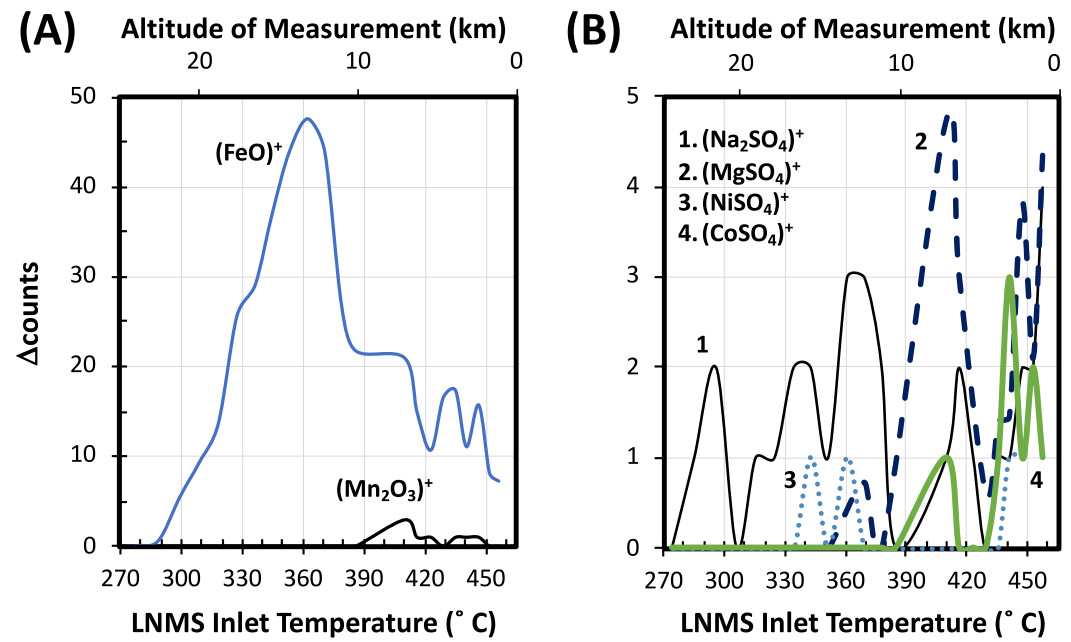

Figure 11. The Large Probe Neutral Mass Spectrometer (LNMS) evolved profiles for (a) FeO^+ and $Mn_2O_3^+$, and (b) $Na_2SO_4^+$, $MgSO_4$, $NiSO_4^+$, and $CoSO_4^+$, where the change in counts (Δcounts), using 24.4 km as the reference, are plotted against the LNMS inlet temperatures (lower *x*-axis) and altitudes of measurement (upper *x*-axis).

Table 7
The LNMS Aerosol Composition Compared to Other Venus Values

LNMS aerosol composition				Comparisons
(A) Bulk aerosol abundances				
Compounds	N ($\times 10^5$)	wt%	mg m^{-3}	mg m^{-3}
Aerosol H_2O	30.02 ± 3.17	62 ± 8	4.2 ± 0.4	–
$Fe_2(SO_4)_3$	0.35 ± 0.05	16 ± 3	1.1 ± 0.2	–
H_2SO_4	1.95 ± 0.28	22 ± 4	1.5 ± 0.2	~0.4–1[a]
Total mass loading			6.8 ± 0.5	~5[b]
(B) Bulk mole ratios				
Compounds	mole ratio	–	–	–
H_2O to $Fe_2(SO_4)_3$	87 ± 16	–	–	–
H_2O to H_2SO_4	15 ± 3	–	–	–
H_2SO_4 to $Fe_2(SO_4)_3$	5.6 ± 1.1	–	–	–
(C) Aerosol constituent abundance				
Constituents	N ($\times 10^5$)	wt%	mg m^{-3}	mg m^{-3}
Total sulfate (SO_4)	2.98 ± 0.32	–	2.2 ± 0.2	>2[c]
Total iron (projected)	1.48 ± 0.71	–	0.3 ± 0.1	0.2 ± 0.1[d]
(D) Aerosol water sources				
T_D	N ($\times 10^5$)	wt%	mg m^{-3}	–
Hydrates T_D ~270–460°C (peak 7, Figure 7) $M_x(SO_4)_y{\cdot}nH_2O$ other hydrates	28.32 ± 3.14	59 ± 8	3.9 ± 0.4	–
Hydrates T_D ~100–270°C (peaks 3–6, Figure 8) $H_2SO_4{\cdot}nH_2O$ $M_x(SO_4)_y{\cdot}nH_2O$	1.58 ± 0.40	3.3 ± 1.0	0.2 ± 0.1	–
Solution Phase T_D ~70–100°C (peak 2, Figure 8)	0.12 ± 0.01	0.2 ± 0.1	0.02 ± 0.01	–
Aerosol H_2O (peaks 2–7, Figures 7 and 8)	30.02 ± 3.17	62 ± 8	4.2 ± 0.4	–
(E) Aerosol volatile fraction				
Compounds	N ($\times 10^5$)	wt%	mg m^{-3}	wt%
H_2SO_4	1.95 ± 0.28	86 ± 17	1.5 ± 0.2	≥75[e]
H_2O	1.73 ± 0.41	14 ± 4	0.2 ± 0.1	–

Note. Aerosols were captured in the LNMS between ~51 and 48 km. The compositional parameters are expressed as number of released molecules (N), weight percentage (wt%), and mass loading (mg m^{-3}). The table is organized by (A) abundances of the major aerosol compounds, (B) bulk mole ratios, (C) bulk abundances of selected constituents, (D) abundances of aerosol H_2O apportioned using the decomposition temperatures (T_D), peak numbers from Figures 7 and 8, and possible sources, including hydrates (e.g., $H_2SO_4{\cdot}nH_2O$ and $M_x(SO_4)_y{\cdot}nH_2O$; M = metal) and the solution phase, and (E) abundances from the volatile fraction of the aerosols. [a]Gel'man et al. (1986); Porshnev et al., (1987). [b]Knollenberg and Hunten (1980); Ragent et al. (1985). [c]Surkov, Ivanova et al. (1986). [d]Andreichikov et al. (1987); Krasnopolsky (1989). [e]Arney et al. (2014) and other works (see Section 3.3).

both instruments collected aerosols and measured the ensuing evolution of O_2 during the thermal decomposition of H_2SO_4.

4. Discussion

4.1. Re-Evaluating the LNMS, LGC, and Other Cloud Probe Measurements

Our combined analyses support the assessment that the LNMS and LGC inadvertently collected and analyzed the contents of Venus' cloud aerosols. Figure 12 illustrates the proposed steps of the unplanned aerosol collection and analysis by the PVLP. These steps included aerosol capture into the LNMS and LGC gas collection assemblies at

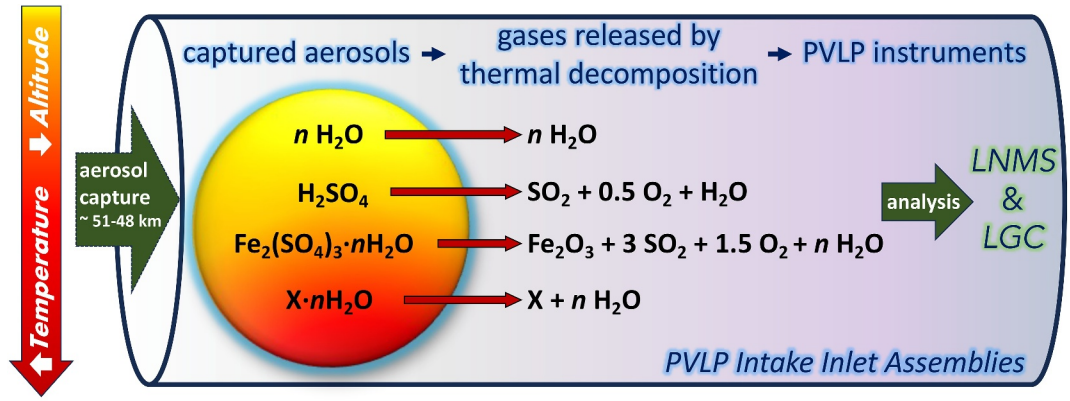

Figure 12. Diagram outlining the capture and analysis of aerosols (yellow sphere) by the Pioneer Venus Large Probe instruments. Aerosol capture in the intake inlet assemblies occurred at ~51–48 km, the aerosol thermal decomposition differentially occurred across the atmosphere, and the decomposition products were released into the Large Probe Neutral Mass Spectrometer and Large Probe Gas Chromatograph. The order of aerosol decomposition included loss of solution-phase H_2O (n H_2O), sulfuric acid (H_2SO_4), hydrated ferric sulfate ($Fe_2(SO_4)_3{\cdot}nH_2O$), and uncharacterized hydrates ($X{\cdot}nH_2O$).

~51–48 km (and possibly on the LIR window), differential thermal decomposition of the aerosol components as the PVLP descended through the hot sub-cloud atmosphere, and the ensuing release of the decomposition products into the LNMS and LGC (and possible release of water vapor off the LIR window). The collection of aerosol particles on the exterior surfaces of the PVLP is suggested by the noted observations for the LIR (Section 3.4). The exterior collection of particles was also considered in Seiff et al. (1995) as the cause of the temperature sensor failure at ~12.5 km.

The unplanned collection and analysis of aerosols were likely not unique to the PVLP. We propose that the cloud sampling instruments onboard the Venera and Vega probes also collected and analyzed the contents of the cloud aerosols. In Sections 4.1.2–4.1.3, the steps of aerosol collection by the LNMS, LGC, and Venera and Vega instruments are summarized. In Sections 4.2–4.5, we discuss the newly identified LNMS mass trends, including the congruent results from the LGC and Venera and Vega instruments, in the context of aerosol composition.

4.1.1. Aerosol Collection and Analysis by the LNMS

Per our understanding of the LNMS project reports (Final Report, Definition Phase Program of the Large Probe Neutral Mass Spectrometer for Pioneer Venus, 1977), the heating profile for the LNMS inlets provided sufficient time for the rapid evaporation of purely volatile aerosol particles after deposition onto the inlet surfaces (e.g., ~10 s for ~100 μm particle). Despite these precautions, the LNMS inlets experienced a significant though temporary clog of the inlets. Hence, this clogging is consistent with the capture of non-volatile aerosol components. Due to the differences between the LNMS and LGC gas collection assemblies (e.g., inlet tube inner dimensions and gas collection mechanisms), the captured aerosols in the LNMS were subjected to much higher temperatures during the descent. As a result, several thermal decomposition products were measured by the LNMS. Most of these products were not characterized in the original LNMS investigations.

Our results support the following assessments: (a) Aerosols predominantly collected within the flattened tips of the LNMS inlets (≤100 nm inner gap) between 51.0 and 48.4 km; (b) The captured aerosols caused substantial though temporary decreases in atmospheric intake (e.g., ~6000-fold decreases in CO_2); (c) The captured aerosols thermally decomposed along the ensuing PVLP descent; (d) The products of aerosol decomposition released into the ion source cavity of the LNMS mass analyzer; and (e) The released products were measured as spikes in the ion counts and ion pump current at the corresponding altitudes of decomposition. The spikes in the ion pump current, which were proportional to the pressure in the mass analyzer, were among the several PVLP anomalies reported by Fimmel (1983) and Seiff et al. (1995). Assignment of these spikes as aerosol decomposition products (e.g., spikes in the pressure in the mass analyzer) represents the first (reported) rational explanation for this apparent LNMS anomaly.

4.1.2. Aerosol Collection and Analysis by the LGC

For the LGC, the collection and analysis of cloud aerosols were considered (Oyama et al., 1979b, Oyama, Carle, Woeller, Pollack et al., 1980) due to the broad and asymmetric peak shapes for H_2O, which were found to be similar between chromatograms obtained in-flight (at 21.6 km) and from laboratory control studies using concentrated H_2SO_4 solution (70.5% by mass). However, the high abundances of SO_2 in the LGC data (at 21.6 km) were not attributed to H_2SO_4 decomposition, since H_2SO_4 decomposition in the LGC was treated as negligible in Oyama et al. (1979b) and Oyama, Carle, Woeller, Pollack et al. (1980). Their evaluation was based on control studies, which showed limited release of SO_2 from SO_3 (a decomposition product of H_2SO_4; Reactions 10 and 11) in analog inlet tubing heated to 160°C (Oyama et al., 1979b). These studies employed typical flow conditions and presumed nominal residence times within the inlet system (Oyama et al., 1979b). However, the effective residence time for the captured aerosols in the LGC was likely up to ∼30 min, when considering the collection of aerosols between ∼51 and 48 km, and the final LGC measurement at 21.6 km.

Therefore, for the LGC, we suggest that: (a) Aerosols collected into the inlet and GSV assembly during descent across ∼51–48 km; (b) The captured aerosols remained adhered in the inlet and GSV across the ∼30-min descent between 51.6 and 21.6 km; (c) In the heated LGC inlet, the captured aerosols thermally decomposed as the PVLP descended deeper into the atmosphere; (d) In the GSV, the captured aerosols dehydrated and partially decomposed due to GSV heating steps (from 60 to 160°C) and appreciable residence times (∼30 min); and (e) The decomposition products from the inlet and GSV were measured as gases with unexpectedly high mixing ratios, asymmetric peak shapes, and/or high uncertainties—such as SO_2, H_2O, and O_2 (Oyama, Carle, Woeller, Pollack et al., 1980).

4.1.3. Aerosol Collection and Analysis by the Venera and Vega Probes

The Venera 13 and 14 and Vega 1 and 2 landers, which sampled and collected gases in the clouds during the descent, likely also inadvertently captured aerosols and measured their contents. The location of atmospheric sampling by the Venera and Vega probes is an important consideration. For example, the GCs and hygrometers on V13/14 and moisture sensors on Vega 1 and 2 sampled within the clouds (Mukhin et al., 1982; Surkov et al., 1982; Surkov, Shcheglov et al., 1986), while the GC on V12 likely began sampling below the clouds (Gel'man et al., 1980). Correspondingly, the cloud measurements obtained high $x$$H_2O$ (∼700–2,000 ppm), while the sub-cloud measurement yielded low $x$$H_2O$ (<100 ppm) (Table 6). These cloud $x$$H_2O$ are further discussed in Section 4.4.

We also propose that the UV spectrometers (ISAV 1 and 2) on Vega 1 and 2 (Bertaux et al., 1996) experienced a partial clog of the intake inlet beginning at ∼52 km in the clouds. Figure 3 aptly demonstrates that clogging of the ISAV 1 and LNMS inlets likely began at similar altitudes (∼51–52 km). These clogs caused ∼4 and 6,000-fold decreases in SO_2 (ISAV 1) and CO_2 (LNMS), respectively. Figure 3 also supports the assessment that the ISAV 1 and LNMS collected aerosols where particle scattering coefficients were highest in the clouds. Unlike the LNMS, the proposed ISAV 1 and 2 clogs rapidly cleared after the probes exited the sub-cloud haze layer. Nominal intake for ISAV 1 and 2 resumed by ∼40 km (Bertaux et al., 1996). This rapid clearing of the clog likely occurred due to the wider inlet and outlet tubes (16 mm, diameter) on ISAV 1 and 2, which were pointed downward and upward during the descent, respectively, and thus subjected to the substantial ram pressures (Bertaux et al., 1996).

Expanding on the interpretations in Bertaux et al. (1996), we propose that after clearing of the ISAV 1 partial clog, a substantial fraction of the collected aerosols remained deposited in the collection tube on the instrumental window and mirrors. These deposited aerosols then underwent thermal decomposition as Vega 1 descended through the sub-cloud atmosphere, since the collection tube was external to the probe and subject to the increasing atmospheric temperatures. The products of the thermal decomposition (e.g., ferric oxide from ferric sulfate and aromatized organic matter of cosmic origin), which increased in abundance across the descent, remained adhered to the window and mirrors. As a result, transmittance through the window decreased, and scattering on the mirrors increased. Per our understanding, the calculations in Bertaux et al. (1996) did not account for any decreases or scattering in incident and/or transmitted light. Instead, the spectrum from ∼62 km was used as the reference incident light for all spectra.

If these inferences are correct, the substantial decreases in $x$$SO_2$ toward the surface reported in Bertaux et al. (1996) (∼120 to 24 ppm from ∼41 to 7 km) do not represent a gradient in atmospheric SO_2 gas. Rather, the

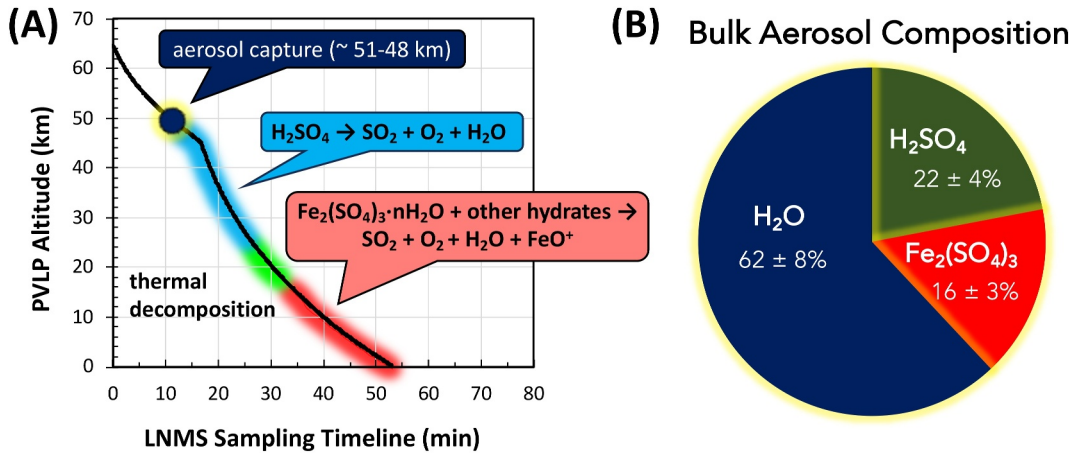

Figure 13. (a) The Large Probe Neutral Mass Spectrometer sampling timeline (~64–0.9 km) showing the elapsed time of aerosol capture and thermal decomposition of H_2SO_4 (blue), short-lived intermediate species (green), hydrated ferric sulfates (e.g., $Fe_2(SO_4)_3 \cdot nH_2O$) (red), and other hydrates (red). (b) Pie chart representing the bulk aerosol composition and abundances.

substantial decreases in xSO_2 were likely the result of over-correction using too high of a reference light intensity. Under these assumptions, the reported decreases in xSO_2 are consistent with the increased darkening of the window and mirrors (per se) resulting from the aerosol decomposition. Later in the descent at ~18 km (Bertaux et al., 1996), a mechanical shock to Vega 1 then released these decomposed materials off the window and mirrors and into the optical pathway, fortuitously yielding the absorption spectra for the aerosol-derived compound/s after partial thermal decomposition. We note that the UV spectra (~250–325 nm) from Bertaux et al. (1996) for the aerosol-derived compound/s are similar, though not identical, to the UV absorption properties of differing ferric sulfates (Egan et al., 2025; Fazl-Ur-Rahman et al., 2021; Jiang et al., 2024) and gaseous polycyclic aromatic hydrocarbons (Sanz-Vicente et al., 1999; Van Engelen et al., 1987).

4.2. Altitude Profiles for SO_2 and H_2O From the LNMS and LGC

The LNMS altitude profiles for xSO_2 and xH_2O show a clear dependence on the capture of aerosols. Prior to aerosol capture (>51.0 km, Figure 4), the LNMS xSO_2 values are consistent with the values based on the PV Orbiter data, which is noteworthy since the PVLP and PV Orbiter concurrently analyzed Venus' atmosphere in 1978. However, after aerosol capture (<51.0 km, Figure 4), the LNMS and LGC xSO_2 and xH_2O (and LIR xH_2O) are substantially higher than the compared spectroscopic measurements (e.g., OS and NIR). In addition, the LNMS profiles for xSO_2 and xH_2O exhibit two maxima at ~35 and 10 km (Figure 4). These observations are inconsistent with interpretation of the LNMS, LGC, and LIR results obtained after aerosol capture as relating to the abundances of atmospheric gases. Moreover, these observations are inconsistent with the assignment of the LNMS H_2O at ~10 km as a terrestrial contaminant, which was proposed in the original LNMS reports (Donahue & Hodges, 1992; Hoffman, Hodges, Donahue, & McElroy, 1980). Rather, the altitude-dependent maxima in the LNMS xSO_2 and xH_2O are consistent with the sequential decomposition of ≥2 sulfate-bearing and hydrated compounds (e.g., $H_2SO_4 \cdot nH_2O$ and metal sulfates ($M_x(SO_4)_y \cdot nH_2O$)). This assessment is highlighted in Figure 4.

4.3. Aerosol Thermal Decomposition Profiles From the LNMS Data

The thermal decomposition profiles from the LNMS data were constructed by considering the number of released molecules, and not mixing ratios, and the temperatures of the inlet assembly, and not altitude. This approach yielded the evolution profiles for SO_2, H_2O, SO_3, O_2, H_xSO_y, and differing metal-bearing species (e.g., FeO^+ and $MgSO_4^+$). These results suggest that the captured aerosols contain—at the minimum—ferric sulfates (e.g., $Fe_2(SO_4)_3$), H_2SO_4, and substantial H_2O arising from hydrates, such as hydrated ferric, magnesium, and other metal sulfates. These hydrates likely formed after capture and thermal evaporation of the aerosols. Figure 13a summarizes the timeline for aerosol capture and sequential thermal decomposition and analysis by the LNMS. Aerosols were captured ~9 min after the beginning of sampling by the LNMS (at ~64 km). Aerosol collection occurred over ~3 min (~51–48 km). The captured aerosols dehydrated and H_2SO_4 decomposed over the

following ~17 min (~48–20 km) and hydrated ferric sulfates and other hydrates predominantly decomposed over the remaining ~23 min of the descent (~20 km to the surface).

4.3.1. Comparing the LNMS, Laboratory, and Venus Thermal Decomposition Profiles

Relative to the LNMS, laboratory studies (on Earth) indicate that higher temperatures are required to release SO_2 from H_2SO_4 gas (>500°C, 1 bar) and ferric sulfates (>550°C, ~1 bar) (Corgnale et al., 2020; Frost et al., 2006; Majzlan et al., 2017; Spratt et al., 2014; Wu et al., 2013; Xu et al., 2010). A rationale for this observation was provided in the original LNMS investigations (Hoffman, Hodges, Donahue, & McElroy, 1980). As explained in Hoffman, Hodges, Donahue, and McElroy (1980), the release of SO_2 from H_2SO_4 was partly replicated using a Venus atmospheric simulator and an LNMS flight spare. In the described control experiments (Hoffman, Hodges, Donahue, & McElroy, 1980), H_2SO_4 was coated onto a tantalum inlet, heated to similar temperatures experienced during the LNMS clog (≤325°C) in the presence of CO_2, and the release of SO_2 and H_2O at ~250°C, including the resumption of flow through the inlet, was confirmed by mass spectral measurements. The control experiments described in Hoffman, Hodges, Donahue, and McElroy (1980) also showed the release of SO_2 after the flow of SO_3 through the tantalum inlet, which likely occurred due to the dissociation of SO_3. These combined results suggest that surface chemistry within the tantalum inlets assisted in H_2SO_4 and SO_3 decomposition. An example surface contribution could include the chemical adsorption of oxygen on the tantalum surfaces (Belov et al., 1978).

Another major factor contributing to the lowered decomposition temperatures is the considerable pressure difference between the ion source cavity of the LNMS (≤10^{-8} bar) and Venus' atmosphere (≤15 bar, ≤25 km). In Corgnale et al. (2020), the release of SO_2 gas from SO_3 (Reaction 11) is described as being favored at low pressures. Reaction 11 is a shared decomposition step for all sulfate-bearing species. Additional contributing factors toward the lowered decomposition temperatures include the acquisition of micron and smaller-sized grains (Archer et al., 2013; Smith et al., 2022), the decomposition of amorphous or partly crystalline materials (Sklute et al., 2018), and instrument geometry (Archer et al., 2013). Formation of sub-micron amorphous or partly crystalline materials is expected in the LNMS inlets during the thermal evaporation of the captured aerosols, which could be predominantly liquid. By extension, these combined contributions may have lowered the effective decomposition temperatures for ferric and other metal sulfates.

At Venus, substantial depletions in atmospheric H_2SO_4 vapor are observed in the sub-cloud atmosphere between ~47 and 35 km (~100–182°C and ~1.6–5.9 bar)—as summarized from chemical models for the lower atmosphere (Bierson & Zhang, 2020; Krasnopolsky, 2007, 2013; Krasnopolsky & Pollack, 1994) and radio occultation studies (Imamura et al., 2017; Jenkins et al., 1994; Kolodner & Steffes, 1998). In the LNMS, H_2SO_4 decomposed over a wider relative altitude range of ~48–25 km, which translated to a heated inlet temperature range of ~102–269°C, compared to a respective atmospheric temperature range of ~93–266°C (Section 2.3 and 2.5). The heated LNMS inlets likely promoted decomposition at higher relative altitudes, while the collection of substantial aerosol materials likely resulted in the decomposition occurring deeper into the lower atmosphere.

4.3.2. Thermal Decomposition of Sulfates and Other Species in the LNMS

The LNMS thermal profiles for SO_2 support the assignments of H_2SO_4 and ferric sulfate as major aerosol components that thermally and differentially decomposed after aerosol capture. In Knollenberg and Hunten (1980), sulfates were suggested to be components of the mode 3 cloud particles. Figures 6–11 show the temperature-dependent evolution profiles for SO_2, H_2O, O_2, SO_3, and differing metal-bearing species such as FeO^+, $MgSO_4^+$, and others. These combined results are consistent with the decomposition of H_2SO_4 and ferric sulfate at roughly 200 and 400°C, respectively. The LNMS data also suggest the presence of sulfides (e.g., H_2S and OCS), other metal sulfates, and P-bearing species.

The assignment of H_2SO_4 is supported by the congruent releases of SO_2 (215°C) (Figure 6), H_2O (185°C) (Figures 7 and 8), and O_2 (205°C) (Figure 9) during the LNMS clog (~50–25 km). For H_2SO_4, the release of H_2O (~185°C) occurred before SO_2 (~215°C), which is consistent with the expected order of gas evolution during the decomposition (e.g., Reaction 10, then Reaction 11). The relative peaks areas for SO_2 and O_2 released during H_2SO_4 decomposition indicate substantial losses of O_2 (>95%), presumably due to reactions with the aerosol components (e.g., organic matter), methane (an in-flight LNMS calibrant), and/or the inner surfaces of the tantalum inlet.

The assignment of ferric sulfate (e.g., $Fe_2(SO_4)_3$) is supported by the congruent releases at the higher temperatures (or deeper into the descent) for SO_2 (397°C; Figure 6), H_2O (414°C; Figures 7 and 8), O_2 (392°C; Figure 9), SO_3 (402°C; Figure 9), various H_xSO_y species (≥340°C; Figure 10a), and FeO^+ (~360 and 405°C; Figure 11a). At these higher temperatures, the maximal release of SO_2 (~397°C) occurred before H_2O (~414°C), suggesting the presence of other hydrates besides hydrated ferric sulfates. No losses in O_2 were observed during the ferric sulfate decomposition. The assignment of ferric sulfates containing hydronium is supported by the release of H_2SO_4 at the higher temperatures. Experimental studies show that H_2SO_4 is a thermal decomposition product of hydronium jarosite ($(H_3O)Fe_3(SO_4)_2(OH)_6$) and rhomboclase ($(H_5O_2)Fe(SO_4)_2{\cdot}2H_2O$), which contains hydronium (H_3O^+) (Frost et al., 2006; Xu et al., 2010). The release of H_2SO_4 from the aerosols at the higher temperatures is supported by the trace spikes (≤20 counts) for $H_2SO_4^+$, $H_2SO_3^+$, and HSO_3^+ (<15 km, or ≥ 340°C, LNMS inlet temperatures) (Figure 10a), which are generally consistent with the electron ionization and fragmentation of H_2SO_4 (Snow & Thomas, 1990).

The release and oxidation of H_2S from the decomposing aerosols is additionally suggested by the LNMS data. The release of sulfenic acid (HSOH) is suggested by the spikes (Figure 10b) for $HSOH^+$, HSO^+, HSO_3^+, and $H_2SO_3^+$ (<20 km; >300°C, LNMS inlet temperatures). These species are generally consistent with the oxidation of sulfides (Berndt et al., 2024; Makarov et al., 2019). Preliminary analyses of the LNMS data reveal increasing H_2S abundances (~14–600 ppm; ~17–2,000 counts) and spikes in the ion counts for COS^+ (≤1,200 counts) and S^+ (≤700 counts) toward the surface (Mogul et al., 2021, Mogul, Limaye & Way, 2023; Zolotov et al., 2023). Similarly, reaction gas chromatography on Vega 2 suggested the release of H_2S and OCS from intentionally captured and heated Venus aerosols (Porshnev et al., 1987). Hence, the LNMS and Vega 2 results suggest the presence of other sulfur and potential carbon species in the aerosols.

The LNMS data additionally suggest the presence of Na_2SO_4, $MgSO_4$, $NiSO_4$, $CoSO_4$, and Mn_2O_3. Trace counts for these metal-bearing species were only present at the higher temperatures (<25 km; >270°C). The detection of trace $Mn_2O_3^+$ is consistent with the thermal decomposition of $MnSO_4$. However, the identification of corroborating counts for $MnSO_4^+$ was not possible, since the corresponding mass (~151 u) was skipped by the preprogrammed LNMS measurement sequence (Section 2.2).

The release of phosphorous acid (H_2PO_3) from the aerosols (and/or lower atmospheric gases) is supported by the respective spikes at ≥420°C at the mass position assigned to $H_2PO_3^+$ and HSO_3^+ (isobaric species), which appear independent of the other $H_xSO_y^+$ species (Figure 10b). Additional support for phosphorus-bearing species was obtained in our preliminary peak fits in the LNMS data (at 31 u), which show trace counts for P^+ at < 25 km (≤30 counts), yet no counts during the clog. However, as shown in Mogul et al. (2021), trace counts of P^+ (≤8 counts) were measured in the clouds before the clog at ~60–50 km (≤8 counts), which is potentially consistent with the tentative detection of phosphorus at ~52–47 km by X-ray radiometry on Vega 1 and 2 (Andreichikov et al., 1987).

4.3.3. Hydrates Suggested by the LNMS Data

The LNMS profiles for H_2O support the abundance of substantial hydrates in the captured aerosols. Given the sequence of aerosol capture and thermal decomposition, the parent mineral species for these hydrates (e.g., metal sulfates, silicates, and/or insoluble organic matter (IOM)) were possibly soluble or particulate species in the aerosols prior to capture. However, a correlation between the aerosol optical properties and hydrate contents is suggested by the congruent relationships between the cloud particle scattering coefficients and cloud H_2O abundances (peaks 1–4, Figure 8).

The minor amounts of H_2O released between ~70 and 270°C (peaks 2–6, Figure 8) likely arose from the solution phase and intermediate hydrates that likely formed during thermal evaporation of the aerosols after capture (e.g., sulfuric acid hydrate and hydrated metal sulfates). The major release of H_2O at ~414°C is consistent with differing hydrates that may have also formed within the LNMS inlets after precipitation or crystallization during the thermal evaporation of the aerosols. The release of H_2O at ~414°C is consistent with (a) the dehydroxylation (e.g., Reactions 12 and 13) of hydronium jarosite at ~300–400°C (Spratt et al., 2014; Šolc et al., 1988), kaolinite ($Al_2Si_2O_5(OH)_4$) at ~400–600°C (Kubliha et al., 2017), and perlite and/or opal (amorphous $SiO_2{\cdot}nH_2O$), containing OH and/or silanol (Si–OH) groups, at ~250–570°C (Thomas et al., 2015), (b) the dehydration of kieserite ($MgSO_4{\cdot}H_2O$) at 390°C (Lauer Jr et al., 2000) and bulk opal at 300–400°C (Thomas et al., 2007), and (c) the pyrolysis of acid-insoluble organic matter (IOM) of cometary/chondritic origin at ~300–450°C (Mimura et al., 2020; Okumura & Mimura, 2011).

Potential detection of $MgSO_4^+$ is consistent with the assignment of kieserite as a source of hydrate-phase H_2O. The presence of Si-Al oxide-rich phases (e.g., kaolinite) and silica-rich materials (e.g., opal) is indirectly supported by the appreciable spike observed in the LNMS CO_2 profile in Figure 3 (demarked by the asterisk at ~440°C or ~3 km). This spike may correspond to SiO^+ (44 u), an isobar to CO_2 (44 u), which could have been released from SiO_2-rich compounds into the LNMS. When considered together, these hydrate-forming and water-liberating compounds (sulfates, oxides, silicates, and IOM) are expected acid alteration products of "rocky" materials delivered to the clouds (Section 4.6).

4.4. Reconciling the Diverse H_2O Measurements in the Clouds

To date, all cloud xH_2O obtained by direct methods (~270–2,400 ppm; PVLP, Venera, and Vega) are much higher than the values obtained by spectroscopy (32 ± 11 ppm). Our work yields unified measurements of water abundances from the PVLP (LNMS, LGC, and LIR). Hence, these total comparisons support the assessment that the cloud measurements obtained by direct and destructive sampling yielded the abundances of H_2O from the captured aerosols. In contrast, spectroscopic measurements yielded the abundances of atmospheric H_2O vapor.

When considering the measurements obtained prior to aerosol capture (>51 km), the results from the PVLP, Venera, and Vega instruments indicate a cloud xH_2O of ≤1,000 ppm (Table 6). As summarized in Figure 4b, this cloud H_2O likely arises from the vapor phase and/or non-clog inducing aerosols. However, after aerosol capture (<51 km), the extreme range in xH_2O obtained by these instruments (~850–16,500 ppm) is likely due to the dissimilarities in the degree of dehydration promoted by the differing sampling profiles. The LNMS was the only cloud probe that continued to analyze samples deeper in the lower atmosphere. As a result, the LNMS sampling sequence encountered the highest atmospheric temperatures and therefore measured the largest evolution of H_2O from the captured aerosols.

To reconcile these diverse measurements of cloud xH_2O (Figures 4b, Table 6), we provide the following explanations for each probe. For the LNMS and LGC, the respective xH_2O at 59.9–51.3 km (~110 ± 12 to 290 ± 30 ppm) and 51.6 km (<600 ppm), which were obtained prior to aerosol capture, represent higher than expected water vapor and/or water released from non-clog inducing hydrates that evaporated at the inlet tips upon capture (Figure 4b). For the LGC, these hydrates could have been collected in the GSV between ~65 and 52 km and subsequently dehydrated at 60°C under the constant flow of carrier gas (He) toward the chromatographic columns (Oyama, Carle, Woeller, Pollack et al., 1980; Oyama, Carle, Woeller, Rocklin et al., 1980).

For the GCs on V13/14, the xH_2O from 58 to 49 km (700 ± 300 ppm) represents the H_2O released from the aerosols captured over a ~9 km collection column, where the collected aerosols likely dehydrated in the GC at a presumed operating temperature of 70°C under the constant flow of carrier gas (Gel'man et al., 1980; Mukhin et al., 1982). For the cloud moisture sensors (52 to 46 km) on V13/14 (2,000 ± 400 ppm H_2O) and Vega 1 and 2 (935 ± 525 ppm H_2O; average and propagated error), the instruments relied on the hygroscopic properties of LiCl (V13/14 and Vega 1 and 2) and P_2O_5 (Vega 1 and 2), which likely acquired H_2O from the captured aerosols (Surkov et al., 1982; Surkov, Shcheglov et al., 1986). Moreover, the high xH_2O from Vega 1 and 2 at ~35 km (~120–140 ppm; Table 6) suggests that a portion of the aerosol H_2O remained adhered in moisture sensors in the sub-cloud atmosphere, despite the constant flow of gases through the inlet and outlet tubes (Surkov, Shcheglov et al., 1986).

For optical spectroscopy (OS) (Ignatiev et al., 1997, 1999), these xH_2O remain to date the only in situ and indirect measurements for H_2O obtained from the middle and lower clouds. This is significant since the OS measurement possesses considerable uncertainties, as described by Ignatiev et al. (1997, 1999). In summary (Ignatiev et al., 1997, 1999), the OS instruments exhibited (a) low resolving powers between H_2O and CO_2, (b) low sensitivity toward H_2O vapor (stated as "saturation of H_2O lines"), and (c) uncertainties in the aerosol model, including an assumption that the cloud aerosols were composed of only H_2SO_4 and H_2O. Figure 10 in Ignatiev et al. (1997) shows the insensitivity of their radiative transfer model toward H_2O vapor. Their calculations showed that ~25-fold increases in H_2O vapor (40–1,000 ppm H_2O) resulted in only ~0.2–fold decreases in irradiance intensities (~3.75–3 at 0.945 μm). Further, in Table 1 and Figure 6 in Ignatiev et al. (1999), the provided errors from ~56 km (8 ± 6 ppm, Table 1) were obtained by comparison to Earth-based experiments and do not represent the errors obtained from their retrieved mixing ratios, which are substantially higher (as shown in their Figure 6). We note that the actual errors from ~50 to 57 km in Ignatiev et al. (1999) are uninterpretable, since they were plotted off the provided scale (0–30 ppm, Figure 6). Hence, the OS xH_2O values for the middle

and lower clouds could be underestimated. This indicates that an assessment of ≤1,000 ppm cloud H_2O vapor, as suggested by the direct PVLP, V13/14, and Vega 1 and 2 measurements, is potentially within the uncertainty limits of the OS xH_2O values.

4.5. Aerosol Composition From the LNMS Data

The LNMS data reveal a novel heterogeneous composition for Venus' aerosols. As visualized in Figure 13b, the captured aerosols contain comparable masses of ferric sulfate (~16 wt% of the total aerosol mass; ~1.1 mg m^{-3}) and H_2SO_4 (~22 wt%; ~1.5 mg m^{-3}), and ~3-fold higher abundances of H_2O arising from hydrates (~62 wt%; ~4.2 mg m^{-3}) (Table 7). An acidic environment containing sufficient H_2O to yield multiple hydrates is consistent with the bulk aerosol mole ratios for $H_2O/Fe_2(SO_4)_3$ (87 ± 16), H_2O/H_2SO_4 (15 ± 3), and $H_2SO_4/Fe_2(SO_4)_3$ (5.6 ± 1.1). These hydrates, which predominantly lost H_2O at ~300–460°C (Table 7), likely formed after capture and thermal evaporation of the aerosols. These hydrates likely include H-bearing ferric sulfates (e.g., containing structural water, hydronium, and/or hydroxyl groups), other thermally stable hydrate species (e.g., kieserite and hydrated sulfates of Na, Ni, Co, and Mn), and/or additional uncharacterized hydrates. Given the impacts of aerosol capture and thermal decomposition, these extracted hydrates may not relate to the mineral identities in the native aerosols.

Our aerosol mass loading values (Figure 13b) are consistent with all prior in situ and remote Venus measurements (Table 7). These congruent values support the assumptions used to estimate the aerosol collection column volume (Sections 2.12 and 3.2). The LNMS value for H_2SO_4 from the volatile fraction of the aerosols (87 ± 17 wt%) is consistent with the abundances of H_2SO_4 (≥75 wt%) inferred from remote polarimetry, in situ polarimetry, and NIR measurements (Arney et al., 2014; Barstow et al., 2012; Hansen & Hovenier, 1974; Knollenberg & Hunten, 1980). The LNMS mass loading for H_2SO_4 in the aerosols (1.5 ± 0.2 mg m^{-3}) is comparable to the abundances of H_2SO_4 (~0.4–1 mg m^{-3}) measured by reaction gas chromatography on Vega 1 and 2 (Gel'man et al., 1986; Porshnev et al., 1987), which likely did not measure reaction products of ferric sulfates, given a limited reactivity with elemental carbon, the reactive agent used in the analysis.

The LNMS mass loading for total sulfate from thermally unstable species (2.2 ± 0.2 mg m^{-3}) is consistent with the mass loading for sulfates (≥2 mg m^{-3} SO_4^{2-}) measured by pyrolysis mass spectrometry on Vega 1, which heated the collected aerosols to 400°C (Surkov, Ivanova et al., 1986). The LNMS mass loading for total Fe (0.3 ± 0.1 mg m^{-3}) is consistent with the tentative mass loading for bulk Fe (0.2 ± 0.1 mg m^{-3}) inferred from X-ray fluorescence measurements on Vega 1 and 2 (Andreichikov et al., 1987). Lastly, the LNMS value for total aerosol mass loading (6.8 ± 0.5 mg m^{-3}) is comparable to measurements from the LCPS on the PVLP (~5 mg m^{-3}; ~51 km) (Knollenberg & Hunten, 1980; Ragent et al., 1985).

4.6. Potential Sources for the Aerosol Components

The LNMS detection of iron species and potentially Mg and Si-bearing compounds in the aerosol phase is consistent with the long-term input of cosmic dust into Venus' atmosphere (Carrillo-Sánchez et al., 2020). Cosmic dust input into Venus' clouds is also suggested by the tentative detection of Fe^+ and Mg^+ in the ionosphere by the PV Orbiter Ion Mass Spectrometer (Taylor Jr et al., 1979). Expected constituents of the cosmic dust include Fe, Mg, Si, Al, Ca, S, and C. While similar constituents are expected from the basaltic dust on Venus' surface (barring C), the transport of particulates to the clouds via atmospheric global circulation, gravity waves, and volcanic plumes remains to be assessed. Currently, there are no measurements of metal content in the deep lower atmosphere or from volcanic plumes on Venus. In Krasnopolsky (2017), vaporous iron chloride from the surface was suggested to rise and ultimately mix with H_2SO_4 in the clouds. However, this hypothesis harbors substantial uncertainties due to a reliance on extrapolated vapor phase properties for iron chloride (Krasnopolsky, 2017). Further, iron oxides, rather than iron chloride, were found to be the stable phases at Venus' surface conditions in Zolotov (2021).

In contrast, the cosmic influx into Venus' atmosphere ($3.2 \pm 1.8 \times 10^4$ kg day^{-1}), as estimated by Carrillo-Sánchez et al. (2020), reaches the total aerosol mass in 3 ± 2 Myr. This suggests sufficient time for chemical alteration, dissolution, and/or suspension of the cosmic material in the H_2SO_4 aerosols (Zolotov et al., 2023). The geologically short residence time of cosmic materials in the clouds implies saturation of clouds with respect to cosmic materials and a net sink toward the surface in the present epoch. Most of the cosmic material that enters Venus' atmosphere consists of cometary dust (Carrillo-Sánchez et al., 2020). While many cosmic compounds (silicates, Fe-Ni metal,

sulfides) dissolve in sulfuric acid, alteration products could include temporarily suspended grains of S_8, silica (e.g., opal), ferric sulfates (e.g., this work; Frankland et al. (2017), Jiang et al. (2024), Krasnopolsky (1989), Krasnopolsky (2017), and Zolotov et al. (2023)), and IOM formed through the incomplete dissolution of high molecular weight organic matter (Alexander et al., 2017; Spacek et al., 2024; Zolotov et al., 2023).

Particle flux of cosmic materials toward the surface likely includes global circulation, degradative loss, and fallout through the hot atmosphere. These processes would likely include (a) evaporation of the aerosol droplets to yield grains of opal, metal sulfates (e.g., Fe, Mg, Ca, Na, Ni, Al, and Co) and silica alumina gel (and/or Al-rich opal), (b) thermal decomposition of the aerosol materials, such as ferric sulfate decomposing to ferric oxide (Reaction 14) and IOM decomposing to C-H-O-N-S gases, graphite, and/or polycyclic aromatic hydrocarbons (as potentially consistent with the Vega 1 results described in Section 4.1.3), and (c) reactions with the hot atmospheric gases (Zolotov, 2018, 2021). Hence, these altered cosmic materials could contribute to the sub-cloud haze (47–30 km) and deep atmospheric dust layers (<20 km), which are observed on Venus (Grieger et al., 2004; Seiff et al., 1995; Titov et al., 2018).

5. Conclusions

The Large Probe Neutral Mass Spectrometer (LNMS) data are the highest resolution mass spectra obtained in Venus' atmosphere to date. In this work, we show that the LNMS data and Large Probe Gas Chromatograph results are consistent with the thermal and evolved gas analysis of aerosol composition. Our results suggest that aerosols from Venus' middle and lower clouds, which were inadvertently captured, possess a heterogeneous composition, where water, ferric sulfate, and sulfuric acid are major components. The mass spectral data suggest that the aerosols contain sufficient water to yield hydrated ferric sulfates, potentially hydrated magnesium sulfate, and other uncharacterized hydrates. However, the exact mineral identities in the native aerosols (pre-capture, thermal evaporation, and decomposition) remain to be assessed. Current efforts aim to elucidate the water activity, acidity, and degree of ferric sulfate hydration and solubility under aerosol conditions.

The assessment that Venus' aerosols contain several major species significantly updates the current perception that the cloud aerosols are composed of concentrated or pure sulfuric acid. These results significantly expand upon the original PVLP investigations. We further propose that unplanned aerosol collection and analysis occurred in all direct measurements conducted thus far in Venus' clouds (e.g., PVLP, Venera, and Vega probes). The unplanned capture of aerosols is consistent with the temporary losses in signal due to inlet clogging for the LNMS and Vega 1 and 2 Ultraviolet Spectrometers. The unplanned analysis of aerosol composition is consistent with the measurement of unexpectedly high-abundant gases, such as SO_2, H_2O, and O_2, by the LNMS, LGC, Venera 13/14 gas chromatographs, Venera 13/14 hygrometers, and Vega 1 and 2 moisture meters.

These assessments of unplanned aerosol collection, including the summaries provided for the PVLP gas collection assemblies, are relevant to the planned DAVINCI mission (Garvin et al., 2022; Yew et al., 2024), which intends to sample within the clouds. The DAVINCI measurements could also rectify uncertainties regarding the abundance of water vapor in the middle and lower clouds. The identification of potential cosmic materials in the aerosols (e.g., Fe, Mg, and Si) is relevant to the selected ISRO Venus Orbiter Mission, which plans to measure the abundance and flux of interplanetary dust particles using the Venus Orbit Dust Experiment (I.S.R.O., 2024; Widemann et al., 2024).

Thus, this work reveals previously underestimated reservoirs of bulk water and possible altered cosmic materials in Venus' aerosols. The sulfuric acid abundances and total aerosol mass loading presented in this study are consistent with all prior Venus measurements. Together, these results provide new considerations for cloud chemistry models and cloud habitability discussions.

Data Availability Statement

The LNMS data are available for download on Zenodo and at the NASA Space Science Data Coordinated Archive (NSSDCA) (Hoffman, 1978a, 1978b). The LNMS data were originally released online by the NSSDCA in 2021 and further described in 2022. The LNMS data were uploaded to Zenodo in 2025. The gas abundances of CO_2, SO_2, and H_2O from this study are available on Zenodo (https://doi.org/10.5281/zenodo.17148805). The laboratory notebooks of J. H. Hoffman (Principal Investigator in the original LNMS project) from 1976 to 1979 are available for download as a collection on Zenodo (Hoffman, 1976–1979). The Hoffman laboratory notebooks

were obtained from the archives at the William B. Hanson Center for Space Sciences, University of Texas, Dallas. The PVLP project reports used in the study, which are currently under ITAR control, are available for review upon request at the NASA Ames Research Center Archives (https://www.nasa.gov/archives/arc-archives/#CollectionsOvw-arc) as part of the Pioneer Project Collection (Acceptance Test Report, 1977; Final Report, Definition Phase Program of the Large Probe Neutral Mass Spectrometer for Pioneer Venus, 1977; Final Report, Large Probe Neutral Mass Spectrometer, 1978; Large & Small Probe Data Book, 1976).

Acknowledgments

We thank David R. Williams from the NASA Space Science Data Coordinated Archive for retrieving and scanning microfilms of the original LNMS data. We thank April Gage (senior archivist) at the NASA Ames Research Center Archives for invaluable assistance with accessing the LNMS and LGC reports in the Pioneer Project Collection. We thank Philip Anderson at the W.B. Hanson Center for Space Sciences at the University of Texas, Dallas for granting access to the LNMS laboratory notebooks of John Hoffman. RM, MYZ, MJW, and SSL acknowledge support (award 80NSSC24K0929) from the Solar Systems Working element of the Research Opportunities in Space and Earth Sciences (ROSES) from the National Aeronautics and Space Administration (NASA). RM acknowledges prior funding from NASA Nexus for Exoplanet System Science (NExSS) program (awards 80NSSC22K1316 and 80NSSC21K1176). RM acknowledges administrative support from the Blue Marble Institute of Science. MYZ was supported by the Discovery and Solar System Workings NASA programs. MJW was supported by the NASA Astrobiology Program through collaborations arising from his participation in the NExSS and the NASA Habitable Worlds Program. MJW also acknowledges support from the GSFC Sellers Exoplanet Environments Collaboration (SEEC), which is funded by the NASA Planetary Science Division's Internal Scientist Funding Model.

References

Acceptance Test Report (LGC #590, PVLGC SN02) [Report]. (1977). NASA; NASA Ames Research Center History Archives (p. 22). Collection Number AFS8100.15A.0000264.

Alexander, C. O. D., Cody, G., De Gregorio, B., Nittler, L., & Stroud, R. (2017). The nature, origin and modification of insoluble organic matter in chondrites, the major source of Earth's C and N. *Geochemistry*, *77*(2), 227–256. https://doi.org/10.1016/j.chemer.2017.01.007

Andreichikov, B. M., Akhmetshin, I., Korchuganov, B., Mukhin, L., & Ogorodnikov, B. (1987). X-ray radiometric analysis of Venus cloud aerosol by VEGA-1 and -2 automated interplanetary probe. *Cosmic Research*, *25*, 721–736.

Archer, P. D., Ming, D. W., & Sutter, B. (2013). The effects of instrument parameters and sample properties on thermal decomposition: Interpreting thermal analysis data from Mars. *Planetary Science*, *2*, 1–21. https://doi.org/10.1186/2191-2521-2-2

Arney, G., Meadows, V., Crisp, D., Schmidt, S. J., Bailey, J., & Robinson, T. (2014). Spatially resolved measurements of H_2O, HCl, CO, OCS, SO_2, cloud opacity, and acid concentration in the Venus near-infrared spectral windows. *Journal of Geophysical Research: Planets*, *119*(8), 1860–1891. https://doi.org/10.1002/2014je004662

Barstow, J., Tsang, C., Wilson, C., Irwin, P., Taylor, F., McGouldrick, K., et al. (2012). Models of the global cloud structure on Venus derived from Venus express observations. *Icarus*, *217*(2), 542–560. https://doi.org/10.1016/j.icarus.2011.05.018

Basner, R., Schmidt, M., Deutsch, H., Tarnovsky, V., Levin, A., & Becker, K. (1995). Electron impact ionization of the SO_2 molecule. *The Journal of Chemical Physics*, *103*(1), 211–218. https://doi.org/10.1063/1.469634

Belov, V., Ustinov, Y. K., & Komar, A. (1978). Carbon monoxide and carbon dioxide interaction with tantalum. *Surface Science*, *72*(2), 390–404. https://doi.org/10.1016/0039-6028(78)90303-5

Berndt, T., Hoffmann, E. H., Tilgner, A., & Herrmann, H. (2024). Gas-phase formation of sulfurous acid (H_2SO_3) in the atmosphere. *Angewandte Chemie International Edition*, *63*(30), e202405572. https://doi.org/10.1002/anie.202405572

Bertaux, J.-L., Widemann, T., Hauchecorne, A., Moroz, V. I., & Ekonomov, A. P. (1996). VEGA 1 and VEGA 2 entry probes: An investigation of local UV absorption (220–400 nm) in the atmosphere of Venus (SO_2 aerosols, cloud structure). *Journal of Geophysical Research*, *101*(E5), 12709–12745. https://doi.org/10.1029/96je00466

Bézard, B., & de Bergh, C. (2007). Composition of the atmosphere of Venus below the clouds. *Journal of Geophysical Research*, *112*(E4), E04S07. https://doi.org/10.1029/2006je002794

Bézard, B., De Bergh, C., Fegley, B., Maillard, J. P., Crisp, D., Owen, T., et al. (1993). The abundance of sulfur dioxide below the clouds of Venus. *Geophysical Research Letters*, *20*(15), 1587–1590. https://doi.org/10.1029/93gl01338

Bierson, C., & Zhang, X. (2020). Chemical cycling in the Venusian atmosphere: A full photochemical model from the surface to 110 km. *Journal of Geophysical Research: Planets*, *125*(7), e2019JE006159. https://doi.org/10.1029/2019je006159

Carrillo-Sánchez, J. D., Gómez-Martín, J. C., Bones, D. L., Nesvorný, D., Pokorný, P., Benna, M., et al. (2020). Cosmic dust fluxes in the atmospheres of Earth, Mars, and Venus. *Icarus*, *335*, 113395. https://doi.org/10.1016/j.icarus.2019.113395

Corgnale, C., Gorensek, M. B., & Summers, W. A. (2020). Review of sulfuric acid decomposition processes for sulfur-based thermochemical hydrogen production cycles. *Processes*, *8*(11), 1383. https://doi.org/10.3390/pr8111383

Donahue, T. M., & Hodges, R. R., Jr. (1992). Past and present water budget of Venus. *Journal of Geophysical Research*, *97*(E4), 6083–6091. https://doi.org/10.1029/92je00343

Dutta, S., Guecha-Ahumada, N., Garrison, M., Hughes, K., & Johnson, M. (2023). DAVINCI Venus entry, descent, and landing modeling and simulation. In *AIAA SCITECH 2023 Forum*, 1165.

Dyson, N. (1998). *Chromatographic integration methods*. Royal Society of Chemistry.

Egan, J. V., James, A. D., & Plane, J. M. C. (2025). Laboratory measurements of ferric chloride ($FeCl_3$) under venusian conditions. *ACS Earth and Space Chemistry*, *9*(8), 2127–2136. https://doi.org/10.1021/acsearthspacechem.5c00132

Esposito, L. W., Bertaux, J.-L., Krasnopolsky, V., Moroz, V., & Zasova, L. (1997). Chemistry of lower atmosphere and clouds. *Venus*, *II*, 415–458. https://doi.org/10.2307/j.ctv27tct5m.18

Fazl-Ur-Rahman, K., Kamath, P. V., & Periyasamy, G. (2021). Spectroscopic and theoretical investigation on the origin of color in jarosites. *Spectrochimica Acta Part A: Molecular and Biomolecular Spectroscopy*, *251*, 119414. https://doi.org/10.1016/j.saa.2020.119414

Fimmel, R. O. (1983). *Pioneer Venus, scientific and technical information branch*. NASA.

Final Report, Definition Phase Program of the Large Probe Neutral Mass Spectrometer for Pioneer Venus [Report]. (1977). NASA Ames Research Center History Archives. Collection Number AFS8100.15A.0000262.

Final Report, Large Probe Neutral Mass Spectrometer [Report]. (1978). University of Texas, Dallas; NASA Ames Research Center History Archives. Collection Number AFS8100.15A.0000261.).

Frankland, V. L., James, A. D., Carrillo-Sánchez, J. D., Nesvorný, D., Pokorný, P., & Plane, J. M. C. (2017). CO oxidation and O_2 removal on meteoric material in Venus' atmosphere. *Icarus*, *296*, 150–162. https://doi.org/10.1016/j.icarus.2017.06.005

Frost, R., Wills, R., Kloprogge, J., & Martens, W. (2006). Thermal decomposition of hydronium jarosite $(H_3O)Fe_3(SO_4)_2(OH)_6$. *Journal of Thermal Analysis and Calorimetry*, *83*(1), 213–218. https://doi.org/10.1007/s10973-005-6908-0

Garvin, J. B., Getty, S. A., Arney, G. N., Johnson, N. M., Kohler, E., Schwer, K. O., et al. (2022). Revealing the mysteries of Venus: The DAVINCI mission. *The Planetary Science Journal*, *3*(5), 117. https://doi.org/10.3847/psj/ac63c2

Gel'man, B., Drozdov, Y. V., Melnikov, V., Rotin, V., Khokhlov, V., Bondarev, V., et al. (1986). Reaction gas chromatography of Venus cloud aerosols. *Soviet Astronomy Letters*, *12*, 42.

Gel'man, B., Zolotukhin, V. G., & Lamonov, B. (1980). An analysis of the chemical composition of the atmosphere of Venus on an AMS of the Venera-12 using a gas chromatograph. *Cosmic Research*, *17*(5), 585–589.

Grieger, B., Ignatiev, N., Hoekzema, N., & Keller, H. U. (2004). Indication of a near surface cloud layer on Venus from reanalysis of venera 13/14 spectrophotometer data. *Proc. Int. Workskhop "Planetary Probe Atmospheric Entry and Descent Trajectory Analysis and Science*, *544*, 63–70.

Hansen, J. E., & Hovenier, J. (1974). Interpretation of the polarization of Venus. *Journal of the Atmospheric Sciences*, *31*(4), 1137–1160. https://doi.org/10.1175/1520-0469(1974)031<1137:iotpov>2.0.co;2

Haus, R., Kappel, D., & Arnold, G. (2015). Lower atmosphere minor gas abundances as retrieved from Venus express VIRTIS-M-IR data at 2.3 μm. *Planetary and Space Science*, *105*, 159–174. https://doi.org/10.1016/j.pss.2014.11.020

Hoffman, J. H. (1976-1979). Laboratory Notebooks for the Pioneer Venus Large Probe Neutral Mass Spectrometer (1976-1979) [Laboratory Notebook Collection]. *Zenodo*. https://doi.org/10.5281/zenodo.15160195

Hoffman, J. H. (1978a). Pioneer Venus large probe: Neutral mass spectrometer, gas sampling tables, 1-15 amu and 15-208 amu [Dataset]. *NASA Space Science Data Coordinated Archive*. NSSDCA ID: PSPA-00649 https://nssdc.gsfc.nasa.gov/nmc/dataset/display.action?id=PSPA-00649

Hoffman, J. H. (1978b). Data from the Pioneer Venus Large Probe Neutral Mass Spectrometer [Dataset]. https://doi.org/10.5281/zenodo.15159583

Hoffman, J. H., Chaney, R. C., & Hammack, H. (2008). Phoenix Mars Mission—The thermal evolved gas analyzer. *Journal of the American Society for Mass Spectrometry*, *19*(10), 1377–1383. https://doi.org/10.1016/j.jasms.2008.07.015

Hoffman, J. H., Hodges, R. R., Donahue, T. M., & McElroy, M. B. (1980). Composition of the Venus lower atmosphere from the Pioneer Venus mass spectrometer. *Journal of Geophysical Research*, *85*(A13), 7882–7890. https://doi.org/10.1029/ja085ia13p07882

Hoffman, J. H., Hodges, R. R., & Duerksen, K. D. (1979). Pioneer Venus large probe neutral mass spectrometer. *Journal of Vacuum Science and Technology*, *16*(2), 692–694. https://doi.org/10.1116/1.570059

Hoffman, J. H., Hodges, R. R., Wright, W. W., Blevins, V. A., Duerksen, K. D., & Brooks, L. D. (1980). Pioneer Venus sounder probe neutral gas mass spectrometer. *IEEE Transactions on Geoscience and Remote Sensing*, *GE-18*(1), 80–84. https://doi.org/10.1109/tgrs.1980.350286

Ignatiev, N., Moroz, V., Moshkin, B., Ekonomov, A., Gnedykh, V., Grigoriev, A., & Khatuntsev, I. (1997). Water vapour in the lower atmosphere of Venus: A new analysis of optical spectra measured by entry probes. *Planetary and Space Science*, *45*(4), 427–438. https://doi.org/10.1016/s0032-0633(96)00143-2

Ignatiev, N., Moroz, V., Zasova, L., & Khatuntsev, I. (1999). Water vapour in the middle atmosphere of Venus: An improved treatment of the Venera 15 IR spectra. *Planetary and Space Science*, *47*(8–9), 1061–1075. https://doi.org/10.1016/s0032-0633(99)00030-6

Imamura, T., Ando, H., Tellmann, S., Pätzold, M., Häusler, B., Yamazaki, A., et al. (2017). Initial performance of the radio occultation experiment in the Venus orbiter mission Akatsuki. *Earth Planets and Space*, *69*(1), 137. https://doi.org/10.1186/s40623-017-0722-3

I.S.R.O. (2024). Union cabinet approves India's mission to Venus, and sample return from the Moon. Retrieved from https://www.isro.gov.in/UnionCabinetApprovesIndiasMission.html

Jenkins, J. M., Steffes, P. G., Hinson, D. P., Twicken, J. D., & Tyler, G. L. (1994). Radio occultation studies of the Venus atmosphere with the Magellan spacecraft: 2. Results from the October 1991 experiments. *Icarus*, *110*(1), 79–94. https://doi.org/10.1006/icar.1994.1108

Jiang, C. Z., Rimmer, P. B., Lozano, G. G., Tosca, N. J., Kufner, C. L., Sasselov, D. D., & Thompson, S. J. (2024). Iron-sulfur chemistry can explain the ultraviolet absorber in the clouds of Venus. *Science Advances*, *10*(1), eadg8826. https://doi.org/10.1126/sciadv.adg8826

Keldysh, M. (1977). Venus exploration with the Venera 9 and Venera 10 spacecraft. *Icarus*, *30*(4), 605–625. https://doi.org/10.1016/0019-1035(77)90085-9

Kim, Y.-K., Irikura, K. K., Rudd, M. E., Ali, M. A., Stone, P. M., Chang, J. et al. (2004). Electron-impact cross sections for ionization and Excitation Database (version 3.0). Retrieved from http://physics.nist.gov/ionxsec

Knollenberg, R., & Hunten, D. (1980). The microphysics of the clouds of Venus: Results of the Pioneer Venus particle size spectrometer experiment. *Journal of Geophysical Research*, *85*(A13), 8039–8058. https://doi.org/10.1029/JA085iA13p08039

Kolodner, M. A., & Steffes, P. G. (1998). The microwave absorption and abundance of sulfuric acid vapor in the Venus atmosphere based on new laboratory measurements. *Icarus*, *132*(1), 151–169. https://doi.org/10.1006/icar.1997.5887

Krasnopolsky, V. (1989). Vega mission results and chemical composition of Venusian clouds. *Icarus*, *80*(1), 202–210. https://doi.org/10.1016/0019-1035(89)90168-1

Krasnopolsky, V., & Pollack, J. (1994). H_2O-H_2SO_4 system in Venus' clouds and OCS, CO, and H_2SO_4 profiles in Venus' troposphere. *Icarus*, *109*(1), 58–78. https://doi.org/10.1006/icar.1994.1077

Krasnopolsky, V. A. (2007). Chemical kinetic model for the lower atmosphere of Venus. *Icarus*, *191*(1), 25–37. https://doi.org/10.1016/j.icarus.2007.04.028

Krasnopolsky, V. A. (2013). S_3 and S_4 abundances and improved chemical kinetic model for the lower atmosphere of Venus. *Icarus*, *225*(1), 570–580. https://doi.org/10.1016/j.icarus.2013.04.026

Krasnopolsky, V. A. (2017). On the iron chloride aerosol in the clouds of Venus. *Icarus*, *286*, 134–137. https://doi.org/10.1016/j.icarus.2016.10.003

Kubliha, M., Trnovcová, V., Ondruška, J., Štubňa, I., Bošák, O., & Kaljuvee, T. (2017). Comparison of dehydration in kaolin and illite using DC conductivity measurements. *Applied Clay Science*, *149*, 8–12. https://doi.org/10.1016/j.clay.2017.08.012

Large and Small Probe Data Book [Report]. (1976). *Hughes aircraft Company*. NASA Ames Research Center History Archives. Collection Number AFS8100.15A.0000063.

Lauer Jr, H., Ming, D. W., Golden, D., Lin, I.-C., Morris, R., & Boynton, W. (2000). Thermal and evolved gas analyses at reduced pressures: A mineral database for the thermal evolved gas analyzer (TEGA). In *31st Lunar and Planetary Science*, 20000085925. Retrieved from https://ntrs.nasa.gov/citations/20000085925

Li, M., Liu, S.-R., & Armentrout, P. (2009). Collision-induced dissociation studies of $Fe_mO_n^+$: Bond energies in small iron oxide cluster cations, $Fe_mO_n^+$ (m= 1–3, n= 1–6). *The Journal of Chemical Physics*, *131*(14), 144310. https://doi.org/10.1063/1.3246840

Linkin, V., Blamont, J., Lipatov, A., Devyatkin, S., Dyachkov, A., Ignatova, S., et al. (1986). Vertical thermal structure in the Venus atmosphere from Provisional VEGA-2 temperature and pressure data. *Soviet Astronomy Letters*, *12*, 40–42.

Lorenz, R. (2025). Engineering models of turbulence in the Venus atmosphere: Application to DAVINCI and other missions. *Planetary and Space Science*, *255*, 106030. https://doi.org/10.1016/j.pss.2024.106030

Lorenz, R. D. (2022). Descent dynamics of the pioneer Venus large probe. In *26th AIAA Aerodynamic Decelerator Systems Technology Conference*, 2742.

Majzlan, J., Grevel, K.-D., Kiefer, B., Nielsen, U. G., Grube, E., Dachs, E., et al. (2017). Thermodynamics and crystal chemistry of rhomboclase, $(H_5O_2)Fe(SO4)_2{\cdot}2H_2O$, and the phase $(H_3O)Fe(SO_4)_2$ and implications for acid mine drainage. *American Mineralogist*, *102*(3), 643–654. https://doi.org/10.2138/am-2017-5909

Makarov, S. V., Horváth, A. K., & Makarova, A. S. (2019). Reactivity of small oxoacids of sulfur. *Molecules*, *24*(15), 2768. https://doi.org/10.3390/molecules24152768

Marcq, E., Amine, I., Duquesnoy, M., & Bézard, B. (2021). Evidence for SO_2 latitudinal variations below the clouds of Venus. *Astronomy and Astrophysics*, *648*, L8. https://doi.org/10.1051/0004-6361/202140837

Marcq, E., Bézard, B., Drossart, P., Piccioni, G., Reess, J., & Henry, F. (2008). A latitudinal survey of CO, OCS, H_2O, and SO_2 in the lower atmosphere of Venus: Spectroscopic studies using VIRTIS-H. *Journal of Geophysical Research*, *113*(E5). https://doi.org/10.1029/2008je003074

Marcq, E., Bézard, B., Reess, J. M., Henry, F., Érard, S., Robert, S., et al. (2023). Minor species in Venus' night side troposphere as observed by VIRTIS-H/Venus express. *Icarus*, *405*, 115714. https://doi.org/10.1016/j.icarus.2023.115714

Markiewicz, W. J., Petrova, E., Shalygina, O., Almeida, M., Titov, D. V., Limaye, S. S., et al. (2014). Glory on Venus cloud tops and the unknown UV absorber. *Icarus*, *234*, 200–203. https://doi.org/10.1016/j.icarus.2014.01.030

McAdam, A., Sutter, B., Archer, P., Franz, H., Wong, G., Lewis, J., et al. (2022). Evolved gas analyses of sedimentary rocks from the glen Torridon clay-bearing unit, Gale crater, Mars: Results from the Mars science laboratory sample analysis at Mars instrument suite. *Journal of Geophysical Research: Planets*, *127*(9), e2022JE007179. https://doi.org/10.1029/2022je007179

McAdam, A. C., Franz, H. B., Sutter, B., Archer Jr, P. D., Freissinet, C., Eigenbrode, J. L., et al. (2014). Sulfur-bearing phases detected by evolved gas analysis of the Rocknest aeolian deposit, gale crater, Mars. *Journal of Geophysical Research: Planets*, *119*(2), 373–393. https://doi.org/10.1002/2013je004518

Mills, F. P., Esposito, L. W., & Yung, Y. L. (2007). Atmospheric composition, chemistry, and clouds, In *Exploring Venus as a Terrestrial Planet* (pp. 73–100). Wiley. https://doi.org/10.1029/176GM06

Mimura, K., Okumura, F., & Harada, N. (2020). Constraints on the thermal history of the Allende (CV3) meteorite by gradual and stepwise pyrolyses of insoluble organic matter. *Geochemical Journal*, *54*(4), 255–265. https://doi.org/10.2343/geochemj.2.0589

Mogul, R., Avice, G., Limaye, S. S., & Way, M. J. (2023). Deriving new mixing ratios for Venus atmospheric gases using data from the Pioneer Venus large probe neutral mass spectrometer. *MethodsX*, *11*, 102305. https://doi.org/10.1016/j.mex.2023.102305

Mogul, R., Limaye, S. S., Way, M., & Cordova, J. A. (2021). Venus' mass spectra show signs of disequilibria in the middle clouds. *Geophysical Research Letters*, *48*(7), e2020GL091327. https://doi.org/10.1029/2020GL091327

Mogul, R., Limaye, S. S., & Way, M. J. (2023). The CO_2 profile and analytical model for the Pioneer Venus large probe neutral mass spectrometer. *Icarus*, *392*, 115374. https://doi.org/10.1016/j.icarus.2022.115374

Monteiro-Carvalho, A. B., Sigaud, L., & Montenegro, E. (2024). O_2^+ production coming from CO_2 single-event electron impact. *Physical Review Letters*, *132*(15), 153002. https://doi.org/10.1103/physrevlett.132.153002

Mu, J., & Perlmutter, D. D. (1981). Thermal decomposition of inorganic sulfates and their hydrates. *Industrial and Engineering Chemistry Process Design and Development*, *20*(4), 640–646. https://doi.org/10.1021/i200015a010

Mukhin, L., Gelman, B., Lamonov, N., Melnikov, V., Nenarokov, D., Okhotnikov, B., et al. (1982). VENERA-13 and VENERA-14 gas chromatography analysis of the Venus atmosphere composition. *Soviet Astronomy Letters*, *8*, 216–218.

Nothwang, G. J. (1980). Pioneer venus spacecraft design and operation. *IEEE Transactions on Geoscience and Remote Sensing*, *GE-18*(1), 5–10. https://doi.org/10.1109/tgrs.1980.350251

Okumura, F., & Mimura, K. (2011). Gradual and stepwise pyrolyses of insoluble organic matter from the Murchison meteorite revealing chemical structure and isotopic distribution. *Geochimica et Cosmochimica Acta*, *75*(22), 7063–7080. https://doi.org/10.1016/j.gca.2011.09.015

Orient, O., & Strivastava, S. (1987). Electron impact ionisation of H_2O, CO, CO_2 and CH_4. *Journal of Physics B: Atomic and Molecular Physics*, *20*(15), 3923–3936. https://doi.org/10.1088/0022-3700/20/15/036

Oschlisniok, J., Häusler, B., Pätzold, M., Tellmann, S., Bird, M. K., Peter, K., & Andert, T. P. (2021). Sulfuric acid vapor and sulfur dioxide in the atmosphere of Venus as observed by the Venus express radio science experiment VeRa. *Icarus*, *362*, 114405. https://doi.org/10.1016/j.icarus.2021.114405

Oyama, V. I., Carle, G. C., & Woeller, F. (1980). Corrections in the Pioneer Venus sounder probe gas chromatographic analysis of the lower Venus atmosphere. *Science*, *208*(4442), 399–401. https://doi.org/10.1126/science.208.4442.399

Oyama, V. I., Carle, G. C., Woeller, F., & Pollack, J. B. (1979a). Venus lower atmospheric composition: Analysis by gas chromatography. *Science*, *203*(4382), 802–805. https://doi.org/10.1126/science.203.4382.802

Oyama, V. I., Carle, G. C., Woeller, F., & Pollack, J. B. (1979b). Laboratory corroboration of the pioneer Venus gas chromatograph analyses. *Science*, *205*(4401), 52–54. https://doi.org/10.1126/science.205.4401.52

Oyama, V. I., Carle, G. C., Woeller, F., Pollack, J. B., Reynolds, R. T., & Craig, R. A. (1980). Pioneer Venus gas chromatography of the lower atmosphere of Venus. *Journal of Geophysical Research*, *85*(A13), 7891–7902. https://doi.org/10.1029/ja085ia13p07891

Oyama, V. I., Carle, G. C., Woeller, F., Rocklin, S., Vogrin, J., Potter, W., et al. (1980). Pioneer Venus sounder probe gas chromatograph. *IEEE Transactions on Geoscience and Remote Sensing*, *18*(1), 85–93. https://doi.org/10.1109/tgrs.1980.350287

Panagakos, N., & Waller, P. (1978). *Second Venus spacecraft set for launch*. NASA News Release. Retrieved from https://ntrs.nasa.gov/citations/19780020162

Petrova, E. V. (2018). Glory on Venus and selection among the unknown UV absorbers. *Icarus*, *306*, 163–170. https://doi.org/10.1016/j.icarus.2018.02.016

Petryanov, I., Andreichikov, B., Korchuganov, B., Ovsyankin, E., Ogorodnikov, B., Skitovich, V., & Khristianov, V. (1981a). Application of the FP filter to study aerosol of the Venus clouds. *Dokl. AN SSSR*, *258*, 57.

Petryanov, I., Andreichikov, B., Korchuganov, B., Ovsyankin, E., Ogorodnikov, B., Skitovich, V., & Khristianov, V. (1981b). Iron in the clouds of Venus. *Soviet Physics - Doklady*, *260*, 834–836.

Pollack, J. B., Dalton, J. B., Grinspoon, D., Wattson, R. B., Freedman, R., Crisp, D., et al. (1993). Near-infrared light from Venus' nightside: A spectroscopic analysis. *Icarus*, *103*(1), 1–42. https://doi.org/10.1006/icar.1993.1055

Porshnev, N., Mukhin, L., Gel'man, B., Nenarokov, D., Rotin, V., Dyachkov, A., & Bondarev, V. (1987). Gas chromatographic analysis of the products of thermal reactions of Venus cloud aerosols on the Vega-1 and 2 automated interplanetary probes. *Cosmic Research*, *2*(5), 549–553.

Ragent, B., Esposito, L. W., Tomasko, M. G., Marov, M. Y., Shari, V. P., & Lebedev, V. N. (1985). Particulate matter in the Venus atmosphere. *Advances in Space Research*, *5*(11), 85–115. https://doi.org/10.1016/0273-1177(85)90199-1

Revercomb, H., Sromovsky, L., Suomi, V., & Boese, R. (1985). Thermal net flux measurements on the Pioneer Venus entry probes. *Advances in Space Research*, *5*(9), 81–84. https://doi.org/10.1016/0273-1177(85)90273-x

Sanz-Vicente, I., Cabredo, S., Sanz-Vicente, F., & Galban, J. (1999). Heated flow-cell for gas phase UV-visible detector in gas chromatography of polycyclic aromatic hydrocarbons. *Chromatographia*, *50*(3–4), 202–208. https://doi.org/10.1007/bf02490652

Seiff, A., DeRose, C. E., & Muirhead, V. U. (1982). Unsteady aerodynamics and motions of the Pioneer Venus probes. *Journal of Spacecraft and Rockets*, *19*(5), 404–411. https://doi.org/10.2514/3.62277

Seiff, A., Kirk, D. B., Young, R. E., Blanchard, R. C., Findlay, J. T., Kelly, G., & Sommer, S. (1980). Measurements of thermal structure and thermal contrasts in the atmosphere of Venus and related dynamical observations: Results from the four pioneer Venus probes. *Journal of Geophysical Research*, *85*(A13), 7903–7933. https://doi.org/10.1029/ja085ia13p07903

Seiff, A., Schofield, J., Kliore, A., Taylor, F., Limaye, S., Revercomb, H., et al. (1985). Models of the structure of the atmosphere of Venus from the surface to 100 kilometers altitude. *Advances in Space Research*, *5*(11), 3–58. https://doi.org/10.1016/0273-1177(85)90197-8

Seiff, A., Sromovsky, L. A., Borucki, W., Craig, R. A., Juergens, D., Young, R. E., & Ragent, B. (1995). *Pioneer Venus 12.5 km anomaly workshop report* (Vol. I). NASA, Ames Research Center.

Sklute, E. C., Rogers, A. D., Gregerson, J. C., Jensen, H. B., Reeder, R. J., & Dyar, M. D. (2018). Amorphous salts formed from rapid dehydration of multicomponent chloride and ferric sulfate brines: Implications for Mars. *Icarus*, *302*, 285–295. https://doi.org/10.1016/j.icarus.2017.11.018

Smith, R., McLennan, S., Sutter, B., Rampe, E., Dehouck, E., Siebach, K., et al. (2022). X-Ray amorphous sulfur-bearing phases in sedimentary rocks of gale crater, Mars. *Journal of Geophysical Research: Planets*, *127*(5), e2021JE007128. https://doi.org/10.1029/2021je007128

Snow, K. B., & Thomas, T. F. (1990). Mass spectrum, ionization potential, and appearance potentials for fragment ions of sulfuric acid vapor. *International Journal of Mass Spectrometry and Ion Processes*, *96*(1), 49–68. https://doi.org/10.1016/0168-1176(90)80041-z

Šolc, Z., Trojan, M., Brandova, D., & Kuchler, M. (1988). A study of thermal preparation of iron (III) pigments by means of thermal analysis methods. *Journal of Thermal Analysis and Calorimetry*, *33*(2), 463–469. https://doi.org/10.1007/bf01913924

Spacek, J., Rimmer, P., Owens, G. E., Cady, S. R., Sharma, D., & Benner, S. A. (2024). Production and reactions of organic molecules in clouds of Venus. *ACS Earth and Space Chemistry*, *8*(1), 89–98. https://doi.org/10.1021/acsearthspacechem.3c00261

Spratt, H., Rintoul, L., Avdeev, M., & Martens, W. (2014). The thermal decomposition of hydronium jarosite and ammoniojarosite. *Journal of Thermal Analysis and Calorimetry*, *115*(1), 101–109. https://doi.org/10.1007/s10973-013-3213-1

Straub, H., Lindsay, B., Smith, K., & Stebbings, R. (1996). Absolute partial cross sections for electron-impact ionization of CO_2 from threshold to 1000 eV. *The Journal of Chemical Physics*, *105*(10), 4015–4022. https://doi.org/10.1063/1.472275

Straub, H., Lindsay, B., Smith, K., & Stebbings, R. (1998). Absolute partial cross sections for electron-impact ionization of H_2O and D_2O from threshold to 1000 eV. *The Journal of Chemical Physics*, *108*(1), 109–116. https://doi.org/10.1063/1.475367

Straub, H., Renault, P., Lindsay, B., Smith, K., & Stebbings, R. (1996). Absolute partial cross sections for electron-impact ionization of H_2, N_2, and O_2 from threshold to 1000 eV. *Physical Review A*, *54*(3), 2146–2153. https://doi.org/10.1103/physreva.54.2146

Surkov, Y., Ivanova, V., Pudov, A., Pavlenko, V., Davydov, N., & Shejnin, D. (1982). Venera 13 and venera 14 measurements of the water vapor content in the Venus atmosphere. *Sov. Astron. Lett.l*, *8*, 223–224.

Surkov, Y. A., Ivanova, V., Pudov, A., Volkov, V., Sheretov, E., Kolotilin, B., et al. (1986b). VEGA-1 Mass spectrometry of Venus cloud aerosols-preliminary results. *Soviet Astronomy Letters*, *12*, 44.

Surkov, Y. A., Shcheglov, O., Ryvkin, M., Sheynin, D., & Davydov, N. (1986a). The water vapor content profile in the Venusian atmosphere according to the results of experiments from Vega 1 and 2. *Journal of Geophysical Research*, *91*(B13), E219–E221. https://doi.org/10.1029/jb091ib13p0e219

Sutter, B., Archer, P., Niles, P., Ming, D., Hamara, D., & Boynton, W. (2024). Organic carbon and Ca-rich carbonate detections in soils of the northern plains, Mars: Evaluation of unreported data from the Mars phoenix Scout's thermal evolved gas analyzer (TEGA). *Journal of Geophysical Research: Planets*, *129*(10), e2024JE008335. https://doi.org/10.1029/2024je008335

Sutter, B., Boynton, W., Ming, D., Niles, P., Morris, R., Golden, D., et al. (2012). The detection of carbonate in the Martian soil at the phoenix Landing site: A laboratory investigation and comparison with the Thermal and evolved Gas Analyzer (TEGA) data. *Icarus*, *218*(1), 290–296. https://doi.org/10.1016/j.icarus.2011.12.002

Tagawa, H. (1984). Thermal decomposition temperatures of metal sulfates. *Thermochimica Acta*, *80*(1), 23–33. https://doi.org/10.1016/0040-6031(84)87181-6

Taylor Jr, H. A., Brinton, H. C., Bauer, S. J., Hartle, R. E., Cloutier, P. A., Michel, F. C., et al. (1979). Ionosphere of Venus: First observations of the effects of dynamics on the dayside ion composition. *Science*, *203*(4382), 755–757. https://doi.org/10.1126/science.203.4382.755

Thomas, P., Heide, K., & Földvari, M. (2015). Water and hydrogen release from perlites and opal: A study with a directly coupled evolved gas analyzing system (DEGAS). *Journal of Thermal Analysis and Calorimetry*, *120*(1), 95–101. https://doi.org/10.1007/s10973-014-4336-8

Thomas, P., Šimon, P., Smallwood, A., & Ray, A. (2007). Estimation of the diffusion coefficient of water evolved during the non-isothermal dehydration of Australian sedimentary opal. *Journal of Thermal Analysis and Calorimetry*, *88*(1), 231–235. https://doi.org/10.1007/s10973-006-8133-x

Titov, D. V., Ignatiev, N. I., McGouldrick, K., Wilquet, V., & Wilson, C. F. (2018). Clouds and hazes of Venus. *Space Science Reviews*, *214*(8), 126. https://doi.org/10.1007/s11214-018-0552-z

Tomasko, M., Doose, L., Smith, P. H., & Odell, A. (1980). Measurements of the flux of sunlight in the atmosphere of Venus. *Journal of Geophysical Research*, *85*(A13), 8167–8186. https://doi.org/10.1029/ja085ia13p08167

Van Engelen, D. L., Thomas, L. C., & Piepmeier, E. H. (1987). Ultraviolet spectrometric detection for gas chromatography of polynuclear aromatic compounds with repetitive spectral scans using absorbance and concurrent fluorescence measurements. *Journal of Chromatography A*, *405*, 191–202. https://doi.org/10.1016/s0021-9673(01)81761-1

Wallace, W. E. (2020). Mass Spectra. In P. J. L. A. W. G. Mallard (Ed.), *NIST chemistry WebBook, NIST standard reference database number 69*. National Institute of Standards and Technology. Gaithersburg MD, 20899. https://doi.org/10.18434/T4D303

Widemann, T., Wilson, C., Breuer, D., Gillmann, C., Smrekar, S. E., & Spohn, T. (2024). Venus: Evolution through time–editorial. *Space Science Reviews*, *220*(4), 1–8. https://doi.org/10.1007/s11214-024-01075-0

Winick, J., & Stewart, A. (1980). Photochemistry of SO_2 in Venus' upper cloud layers. *Journal of Geophysical Research*, *85*(A13), 7849–7860. https://doi.org/10.1029/ja085ia13p07849

Wu, H., Jespersen, J. B., Frandsen, F. J., Glarborg, P., Aho, M., Paakkinen, K., & Taipale, R. (2013). Modeling of ferric sulfate decomposition and sulfation of potassium chloride during grate-firing of biomass. *AIChE Journal*, *59*(11), 4314–4324. https://doi.org/10.1002/aic.14174

Xu, W., Parise, J. B., & Hanson, J. (2010). $(H_3O)Fe(SO_4)_2$ formed by dehydrating rhomboclase and its potential existence on Mars. *American Mineralogist*, *95*(10), 1408–1412. https://doi.org/10.2138/am.2010.3470

Yan, B., Li, L., Yu, Q., Hang, W., He, J., & Huang, B. (2010). High irradiance laser ionization mass spectrometry for direct speciation of iron oxides. *Journal of the American Society for Mass Spectrometry*, *21*(7), 1227–1234. https://doi.org/10.1016/j.jasms.2010.02.030

Yew, A. G., Malespin, C. A., & Garvin, J. B. (2024). Pipeline design for Venus mass spectrometer using axial dispersion residence time distributions. *Journal of Thermophysics and Heat Transfer*, *39*(2), 1–7. https://doi.org/10.2514/1.t7026

Zolotov, M. Y. (2018). Gas–solid interactions on Venus and other solar system bodies. *Reviews in Mineralogy and Geochemistry*, *84*(1), 351–392. https://doi.org/10.2138/rmg.2018.84.10

Zolotov, M. Y. (2021). Iron salts and oxides in the history of the surface-atmosphere-cloud System on Venus. In *52nd Lunar and Planetary Science Conference*. Retrieved from https://www.hou.usra.edu/meetings/lpsc2021/pdf/2615.pdf.2615.

Zolotov, M. Y., Mogul, R., Limaye, S. S., Way, M. J., & Garvin, J. B. (2023). Venus cloud composition suggested from the Pioneer Venus large probe neutral mass spectrometer data. In *54th Lunar and Planetary Science Conference*, 2806. Retrieved from https://www.hou.usra.edu/meetings/lpsc2023/pdf/2880.pdf